ESD-TR-72-364

DRI File Copy

ESD ACCESSION LIST
DRI Call No. 78851
Copy No. 1 of 1 cys.

2

# Optics Research

1972

Prepared for the Advanced Research Projects Agency
and the Department of the Air Force
under Electronic Systems Division Contract F19628-73-C-0002 by

Lincoln Laboratory

MASSACHUSETTS INSTITUTE OF TECHNOLOGY

LEXINGTON, MASSACHUSETTS

ESD RECORD COPY
RETURN TO
SCIENTIFIC & TECHNICAL INFORMATION DIVISION
(DRI), Building 1435

AD762320

Approved for public release; distribution unlimited.

2

# Optics Research

1972

Issued 23 May 1973

Prepared for the Advanced Research Projects Agency
and the Department of the Air Force
under Electronic Systems Division Contract F19628-73-C-0002 by

**Lincoln Laboratory**

MASSACHUSETTS INSTITUTE OF TECHNOLOGY

LEXINGTON, MASSACHUSETTS

Approved for public release; distribution unlimited.

The work reported in this document was performed at Lincoln Laboratory, a center for research operated by Massachusetts Institute of Technology. This work was sponsored in part by the Advanced Research Projects Agency of the Department of Defense (ARPA Order 600) and in part by the Department of the Air Force under Contract F19628-73-C-0002.

This report may be reproduced to satisfy needs of U.S. Government agencies.

Non-Lincoln Recipients

**PLEASE DO NOT RETURN**

Permission is given to destroy this document when it is no longer needed.

ABSTRACT

This report covers work of the Optics Division at Lincoln Laboratory for the period 1 July through 31 December 1972. The topics covered are laser technology and propagation, and optical measurements and instrumentation.

Additional information on the optics program may be found in the semi-annual technical summary reports to the Advanced Research Projects Agency.

Accepted for the Air Force
Joseph J. Whelan, USAF
Acting Chief, Lincoln Laboratory Liaison Office

CONTENTS


Abstract iii
Introduction v
Reports on Optics Research vii
Organization ix

I. LASER TECHNOLOGY AND PROPAGATION 1

A. Laser Propagation Through a Turbulent Medium 1

B. Particle-Induced Breakdown of Air in a 10.6-μm Laser Beam 1

1. Long-Pulse Breakdown at 10.6 μm 1
2. Particle-Induced Breakdown in Aerosol 6
3. Aerosol Clearing with a 10.6-μm Precursor Pulse 7
4. Momentum Transfer to Small Particles Irradiated by a Laser 10
5. Characterization of Breakdown Data 12

C. Laser Device Technology 13

1. 500-J E-Beam-Excited Laser 13
2. Optical Output Characteristics of 500-J Pulsed Laser 13
3. E-Beam Laser Kinetics 15
4. E-Beam Laser-Pulse Shaping 19
5. Observation of Laser Oscillation in a 1-atm $CO_2$-$N_2$-He Laser Pumped by an Electrically Heated Plasma Generated via Photoionization 20
6. Large Photoionization Laser 25
7. Laser Power Amplifier Study 36
8. $C^{13}O_2^{16}$ Isotope Lasers 36

II. OPTICAL MEASUREMENTS AND INSTRUMENTATION 41

A. A Very Rapid Interferometric Technique for Visible and IR MTF Measurements 41

B. Atmospheric Optical Coherence Measurements at 10.6 and 0.63 μm 43

1. Visible Measurements 45
2. 10.6-μm Measurements 45
3. Comparison of Visible and 10.6-μm Measurements 49
4. Summary 51

# INTRODUCTION

## I. LASER TECHNOLOGY AND PROPAGATION

Improved calculations are reported of a laser beam passing through a simulated turbulent atmosphere to include cross correlations between different frequency components which should properly account for low spatial frequency effects.

Breakdown initiated on 6- to 100-μm fibers with $CO_2$ laser pulse intensities of $10^6$ to $10^7$ W/cm$^2$ was investigated. Measured parameters included breakdown threshold, time to breakdown, plasma expansion dynamics, and transmission of 10.6-μm laser radiation through the plasma.

Breakdown thresholds for particle-induced breakdowns have been measured for a variety of materials and particle sizes. These are discussed in terms of the material parameters.

The breakdown threshold for a laser pulse in aerosol was increased by application of a low-intensity, high-fluence precursor pulse. Two conditions were investigated: a known distribution, and one large particle (50-μm diameter) in the beam focus. The threshold increases were a factor of 4 and 20, respectively. The most likely mechanism for this was the jetting of large particles out of the beam.

A detailed analysis is given of the jetting process caused by a low-intensity, high-fluence precursor. The measured initial velocity and its rate of decrease agree quite well with the material-coupling and atmospheric-drag coefficients. The maximum velocity measured is shown to be limited by the finite beam size to a factor of 3 below the theoretical maximum.

A correlated summary is given of various data of breakdown in particle-laden air induced by lasers.

The Lincoln Laboratory 500-J E-beam-excited laser first operated successfully in August and has demonstrated a capability for outputs in excess of 600 J. Performance of the laser has been in satisfactory agreement with predictions, and the device is presently in active use in the surface effects and propagation programs.

Measurements have been made of the output power, energy, and approximate beam quality of the Lincoln Laboratory $CO_2$ pulsed E-beam laser. A nearly diffraction-limited beam has been measured using grating-generated burn patterns. To date, 760 ± 100 J of focused energy have been measured.

The kinetics code was refined to include photon time decay effects and the effect of finite vibrational equilibration time of the $\nu_1$ mode. Computations were performed to test theoretically a proposal for eliminating the initial spike by temporally shaping the electron beam.

Work was completed on externally pulsed shaping a $CO_2$ laser. Absorbers were used to generate ramp-shaped pulses or to eliminate or accentuate the initial spike as desired. Preliminary efforts were also made to use the Febetron-excited laser for short-pulse generation and in a passively Q-switched mode.

The photoionization of large organic molecule, tri-n-propylamine, mixed with a 1-atm $CO_2$-$N_2$-He gas is used to produce a high-electron-density, uniform, large-volume laser plasma, via flashlamp illumination. Electron density on the order of $10^{13}/cm^3$ is obtained. The electrons are heated by an externally applied electric field less intense than that required to produce avalanche breakdown. Laser oscillation is observed at the P(20) line of the 10.6-μm $CO_2$ band with a maximum output of 300 mJ obtained from a 0.02-liter active volume (corresponding to 15 J/liter).

An effort has been started to build a several-hundred-joule-per-pulse photoionization-excited laser. Experiments and calculations are reported on initial seed-molecule absorption spectroscopy, flashlamp emission spectroscopy, and cavity illumination techniques.

Feasible laser amplifiers are described to amplify by 33 dB pulses to energies of 200 J in 100 μsec at 10.6 μm in both unsaturated and saturated modes of operations. The parameter studies involved in the evolution of the designs are described. The limiting case of a CW laser for sufficiently fast flow is described for the kinetics of a $CO_2$-$N_2$-He system.

The wavelengths of 72 lasing transitions of $C^{13}O_2^{16}$ lasers were measured. Heterodyning the outputs of $C^{12}O_2^{16}$ and $C^{13}O_2^{16}$ lasers resulted in observation of beat note frequencies up to 18 GHz in the preliminary experiments.

## II. OPTICAL MEASUREMENTS AND INSTRUMENTATION

A triangular-type shearing interferometer for very rapid MTF measurements has been designed. This system, intended for airborne applications, can obtain the complete MTF curve in the order of milliseconds. Using appropriate components and detectors, both visible and infrared (to the 10-μm region) measurements are possible.

Focused spot characteristics and the atmospheric modulation transfer function (MTF) have been measured over a 5.4-km horizontal path with laser light at 0.63 and 10.6 μm. In verification of theory, the inferred atmospheric coherence diameter has been shown to be proportional to $\lambda^{6/5}$ under poor seeing conditions. The atmospherically degraded long-exposure 10.6-μm spot shape was Gaussian, and the spot wander exhibited a stronger dependence on turbulence strength relative to spot blur than was theoretically predicted. The diurnal cycles of the 10.6-μm spot characteristics, and of the 10.6- and 0.63-μm atmospheric MTFs under clear-sky conditions, were also observed.

REPORTS ON OPTICS RESEARCH

1 July through 31 December 1972

## PUBLISHED REPORTS

### Journal Articles*

| JA No. | | | |
|---|---|---|---|
| 3954 | Stability of Two-Dimensional Recursive Filters | T. S. Huang | IEEE Trans. Audio Electroacoust. AU-20, 158 (1972), DDC AD-752937 |
| 3976 | TEA Laser Medium Diagnostics | R. W. O'Neil<br>R. J. Carbone<br>H. Granek<br>H. Kleiman | Appl. Phys. Letters 20, 461 (1972), DDC AD-752950 |
| 4006 | Tunable-Laser Spectroscopy of the $\nu_1$ Band of $SO_2$ | E. D. Hinkley<br>A. R. Calawa<br>P. L. Kelley<br>S. A. Clough† | J. Appl. Phys. 43, 3222 (1972), DDC AD-752967 |
| 4022 | Excitation of a Long-Pulse $CO_2$ Laser with a Short-Pulse Longitudinal Electron Beam | S. Marcus | Appl. Phys. Letters 21, 18 (1972), DDC AD-752953 |
| 4040 | Tunable Infra-red Lasers and Their Applications to Air Pollution Measurements | E. D. Hinkley | Opto-electronics 4, 69 (1972) |
| 4041 | The Feasibility of Producing Laser Plasmas Via Photoionization | A. Javan†<br>J. S. Levine | IEEE J. Quantum Electron. QE-8, 827 (1972), DDC AD-753308 |
| 4041B | The Possibility of Generating Laser Plasmas by Photoionization | A. Javan†<br>J. S. Levine | Phys. Letters B 42B, 173 (1972) (Amsterdam, Netherlands) |
| 4047 | Fog Droplet Vaporization and Fragmentation by a 10.6-μm Laser Pulse | P. Kafalas<br>A. P. Ferdinand, Jr. | Appl. Opt. 12, 29 (1973), DDC AD-758948 |
| 4079 | Lamb Dip in CO Lasers | C. Freed<br>H. A. Haus† | IEEE J. Quantum Electron. QE-9, 219 (1973), DDC AD-758943 |

*Reprints available.

†Author not at Lincoln Laboratory.

| JA No. | | | |
|---|---|---|---|
| 4131 | Observation of Laser Oscillation in a 1-Atm $CO_2$-$N_2$-He Laser Pumped by an Electrically Heated Plasma Generated via Photoionization | J. S. Levine<br>A. Javan* | Appl. Phys. Letters 22, 55 (1973) |
| MS-3146 | Infrared Detectors and Applications | J. O. Dimmock | J. Electronic Materials 1, 255 (1972) |

## UNPUBLISHED REPORTS

### Journal Articles

| JA No. | | | |
|---|---|---|---|
| 4088 | High-Energy Pulsed $CO_2$ Laser Target Interactions in Air | J. E. Lowder<br>D. E. Lencioni<br>T. W. Hilton<br>R. J. Hull | Accepted by J. Appl. Phys. |
| 4121 | Dynamics and Energetics of the Explosive Vaporization of Fog Droplets by a 10.6-μm Laser Pulse | P. Kafalas<br>J. Herrmann | Accepted by Appl. Opt. |

### Meeting Speeches†

| MS No. | | | |
|---|---|---|---|
| 3349A | Detection of Air Pollutants with Tunable Lasers | E. D. Hinkley | First European Electro-Optics Markets and Technology Conference and Exhibition, Institut fur Technisch Physik, IPO, Geneva, Switzerland, 12-15 September 1972 |
| 3409 | Atmospheric Optical Coherence Measurements at 10.6 μm and 0.63 μm | T. J. Gilmartin<br>J. Z. Holtz | Optical Society of America, San Francisco, 17-20 October 1972 |
| 3425 | Tunable Semiconductor Diode Lasers and Their Applications | E. D. Hinkley | Tunable Laser Conference, Institute of Physics, Edinburgh, Scotland, 6-8 September 1972 |
| 3433 | Capabilities and Limitations of Infrared Imaging Systems | J. O. Dimmock | SPIE Conference, San Francisco, 16-18 October 1972 |
| 3440 | Laser Air Pollution Measurements | E. D. Hinkley | Seminar, Northeastern University, Boston, 5 December 1972 |
| 3457 | Tunable Laser Air Pollution Detection | E. D. Hinkley | Joint Meeting of '72 International IEEE/G-AP and USNC/URSI, Williamsburg, Virginia, 11-15 December 1972 |

*Author not at Lincoln Laboratory.

† Titles of Meeting Speeches are listed for information only. No copies are available for distribution.

# ORGANIZATION

## OPTICS DIVISION

R. H. Rediker, *Head*
L. B. Anderson, *Associate Head*
M. J. Hudson, *Assistant*

## LASER TECHNOLOGY

S. Edelberg, *Leader*
L. C. Marquet, *Associate Leader*

Bradley, L. C.
Brennan, M. J.
Bushee, J. F., Jr.
Ferdinand, A. P., Jr.
Granek, H.
Herrmann, J.
Johnson, J. Q.
Kafalas, P.
Kilcline, C. W.
Kleiman, H.
Kramer, R.
Lencioni, D. E.
Levine, J. S.
Lowder, J. E.
Marcus, S.
Morency, A. J.
O'Neil, R. W.
Pettingill, L. C.
Pike, H. A.
Pirroni, J. S.
Pitts, R. F.
Shey, S. Y.
Theriault, J. R.
Valcourt, G. L.
Weir, D. G.

## ADVANCED SENSORS

J. O. Dimmock, *Leader*
E. S. Cotton, *Associate Leader*
T. M. Quist, *Assistant Leader*

Ariel, E. D.
Baukus, J. P.
Bielinski, J. W.
Bollman, R. A.
Dickey, D. H.
Ellis, R. H.
Fulton, M. J.
Hinkley, E. D.
Kelsall, D.
Marshall, A. P.
Merrill, E. R.
Mudgett, D. A.
Nork, L. P.
Page, D. A.
Perry, F. H.
Sample, J. O.
Rotstein, J.
Scouler, W. J.
Sullivan, F. M.
Swedberg, J. L.
Thomas, M. A.
Wainwright, E. S.
Ziegler, H. L.
Zwicker, H. R.

## OPTO-RADAR SYSTEMS

A. B. Gschwendtner, *Leader*

Bauer, J. R.
Billups, R. R.
Brownson, J. S.
Bryant, B. W.
Clay, W. G.
Coles, R. M.
DiMarzio, E. W.
Dyjak, C. P.
Edwards, D. M.
Garavano, L. A.
Hull, R. J.
Longaker, P. R.
McPhie, J. M.
Stevens, R. R.
Zieman, H. E.

## LASER SYSTEMS

R. H. Kingston, *Leader*
L. J. Sullivan, *Associate Leader*

Bates, D. H.
Bicknell, W. E.
Capes, R. N., Jr.
Chaulk, L. W.
Daley, J. A., Jr.
Freed, C.
Gilmartin, T. J.
Holtz, J. Z.
Huang, T. S.
Malling, L. R.
Marapoti, J. V.
O'Donnell, R. G.
Parker, A. C.
Swezey, L. W.
Teoste, R.
Zimmerman, M. D.

# I. LASER TECHNOLOGY AND PROPAGATION

## A. LASER PROPAGATION THROUGH A TURBULENT MEDIUM

In the previous Optics Research Report,[1] we reported calculations for a laser beam passing through a simulated turbulent atmosphere. Although the simulation of the atmosphere was reasonably good at high spatial frequencies, it did not reproduce low frequencies well because we neglected any cross correlation between components of different frequencies. As a result, tilt and refocusing of the wavefront were considerably underestimated.

We are now engaged in properly incorporating cross correlations into our code. This involves finding the eigenvalues and eigenfunctions of the Fredholm equation

$$\int R(\vec{r}, \vec{r}')\, \psi(\vec{r}')\, d^2r' = \lambda\psi(r)$$

where the kernel $R(\vec{r}, \vec{r}')$ is the autocorrelation of the optical path difference $\int ndz$, and the integral extends over the entire mesh used in the computation.[2] This can be reduced to a matrix eigenvalue problem by expanding the unknown function $\psi$ in a series of orthonormal functions. In principle, any set of functions may be chosen that are complete in the region of interest; in practice, one wishes to choose a set that is as close to the eigenfunctions $\psi$ as possible. We have chosen the Zernike polynomials as basis functions, since they have the right angular dependence to correspond to an isotropic autocorrelation, and the off-diagonal matrix elements are comparatively small.

L. C. Bradley
J. Herrmann

## B. PARTICLE-INDUCED BREAKDOWN OF AIR IN A 10.6-μm LASER BEAM

Three areas have been investigated with regard to the problem of breakdown in air caused by particles: the material dependence of breakdown for breakdown in the short-pulse case (200 nsec), details of fiber-induced breakdown for long pulses, and the possibility of increasing the threshold in aerosol by application of a precursor.

### 1. Long-Pulse Breakdown at 10.6 μm

The observation[3] of air breakdown initiated by airborne particulates after heating times on the order of 10 μsec in a low-intensity $CO_2$ laser beam suggests this phenomenon is an important area of investigation. In the present experiments, we investigated long-pulse breakdown initiated on glass fibers with diameters from 6 to 100 μm. Some threshold measurements were also made with tungsten, beryllium copper, and stainless-steel fibers, and with a plain quartz surface.

The experiment consisted of irradiating fibers suspended in the focal volume of various mirrors with the output from a small E-beam ionized $CO_2$ laser and observing the time development of the breakdown. In some cases, photographs were taken with a high-speed framing camera. The laser was developed by S. Marcus[4] and had an output of about 10 J in a 10- to 20-times diffraction-limited beam. The energy density profile of the focused beam was determined by attenuating the incident beam with fine perforated screens and observing the resulting burn areas on exposed Polaroid film. This procedure was used to determine the peak energy density as a function of the total energy for the three focal length mirrors used in the experiment. The pulse

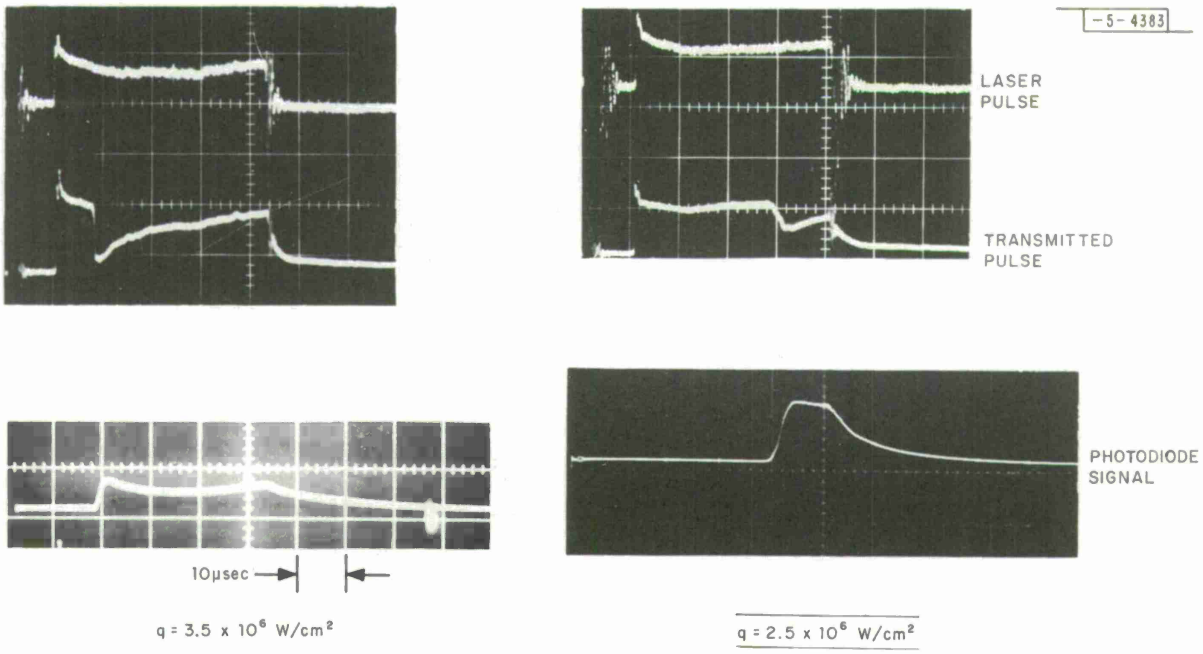


Fig. I-1. Incident and transmitted laser pulses and photodiode signal resulting from breakdown on 30-μm-diameter glass fiber. Laser beam was focused with 20-cm focal-length mirror which yielded focal spot diameter of 0.2 cm.

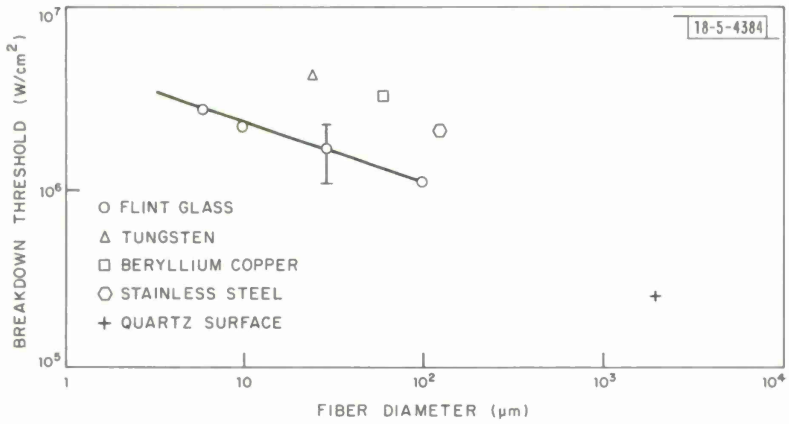


Fig. I-2. Breakdown threshold vs fiber diameter for various materials. Laser beam was focused with 20-cm focal-length mirror.

shape was nearly rectangular, and the pulse length was varied from 20 to 80 μsec by varying the sustainer voltage. Incident pulse shape and energy were monitored with a photon drag detector and a barium titanate energy transducer. The pulse shape transmitted through the focal volume was also monitored with a photon drag detector. Breakdown initiation was detected with a photodiode which viewed the focal volume and by observing the initiation of absorption in the transmitted laser pulse. Typical incident and transmitted laser pulses are shown in Fig. I-1 for breakdown on a 30-μm glass fiber. The dip in the transmitted pulse indicates that absorption of the laser pulse in the breakdown plasma is coincident with the plasma emission recorded by a photodiode.

The breakdown threshold for glass fibers and various metals is shown to decrease in Fig. I-2 as the fiber diameter is increased. The solid line through the glass data indicates a relationship of the form $q \sim (D)^{-1/3}$. The decreased threshold with increased fiber size is believed to be due to the larger 10.6-μm absorption coefficient which results from an increased vapor density in the focal volume due to decreased transverse mass loss. The threshold for a plane surface oriented perpendicular to the laser-beam axis is the limit of this process for a given focal spot size since the blowoff is normal to the surface and mass loss is minimized. The higher thresholds for the metals is due in part to their much higher reflectivity. The cross, which indicates the breakdown threshold observed on a quartz surface, is plotted at the diameter of the focal spot.

The time required to reach breakdown at a constant power density is shown in Fig. I-3 for 100-μm-diameter glass fibers. The solid line indicates a relationship of the form $q \sim (t)^{-0.65}$ The different symbols indicate data taken with focal spot sizes corresponding to various focal-length mirrors used to focus the laser beam. The focal spot diameters were 0.1, 0.2, and 0.4 cm for the 10-, 20-, and 30-cm focal-length mirrors.

The time to reach breakdown is the time required to reach a condition of steady-state vaporization of the fiber plus the time required to heat the vapor to a "threshold temperature" such

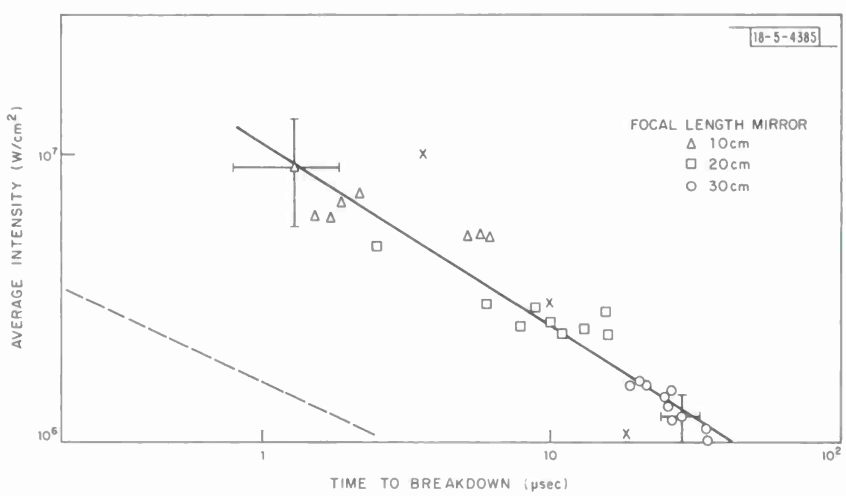


Fig. I-3. Time to breakdown for 100-μm-diameter glass fibers suspended in focal volumes of various focal-length mirrors. Solid line is "best fit" to data, and error bars indicate uncertainty in data. Dashed line is time to reach steady-state vaporization, and symbol X indicates vapor residence time in various focal volumes.

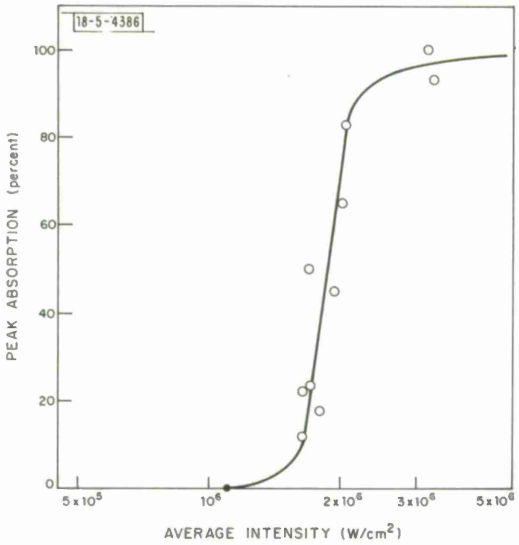


Fig. I-4. Peak attenuation of incident laser beam in breakdown plasmas initiated on 100-μm-diameter glass fibers. Laser beam was focused with 20-cm focal-length mirror.

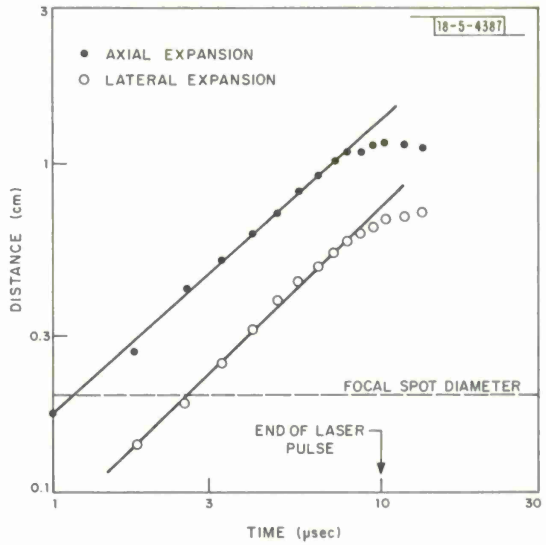


Fig. I-5. Plasma growth as function of time for laser intensity of $2.2 \times 10^6$ W/cm$^2$. Breakdown was initiated on 30-μm-diameter glass fiber after about 40 μsec. Laser beam was focused with 20-cm focal-length mirror. Time scale is indicated from beginning of breakdown.

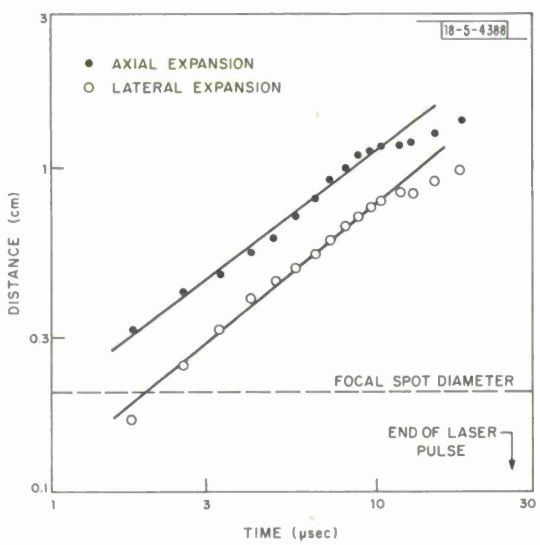


Fig. I-6. Plasma growth as function of time for laser intensity of $2.2 \times 10^6$ W/cm$^2$. Breakdown was initiated on 30-μm-diameter fiber after about 27 μsec. Laser beam was focused with 20-cm focal-length mirror. Time scale is indicated from beginning of breakdown.

that absorption of laser energy by the inverse bremsstrahlung process very quickly produces a highly ionized plasma. If the vapor leaves the focal volume before being heated to the threshold temperature, then breakdown does not occur. As the incident laser intensity is increased, the surface temperature and the rate of vaporization are increased along with the vapor heating rate. The time a vapor molecule can spend in the focal volume is of the order of $\tau \sim D/c$, where D is the focal spot diameter and c is the speed of sound in the heated vapor. The vaporization temperature, and hence the speed of sound in the vapor, is a weak function of the laser intensity so that the vapor heating rate increases faster than the vapor efflux from the focal volume, and leads to breakdown in the vapor with increasing laser intensity. The time to reach steady-state ablation is given by (see Ref. 5 for example)

$$\tau_s \simeq \kappa\left(\frac{\rho L}{q}\right)^2 \tag{I-1}$$

where $\kappa$ is the thermal diffusivity, $\rho$ is the density, L is the heat of vaporization of the glass, and q is the incident laser intensity. With the use of average handbook values for the thermal properties of flint glass, Eq. (I-1) gives the dashed line in Fig. I-3. These calculations indicate that the time to reach steady-state vaporization is short compared with the observed time to breakdown. The time a vapor molecule remains in the focal volume was estimated by assuming the glass vapor was diatomic (SiO and $O_2$) with an average molecular weight of 40, and that the vaporization temperature ranged from 3100° to 3700°K for laser intensities from $10^6$ to $10^7$ W/cm$^2$ (Ref. 5). Approximate focal volume residence times were calculated for each focal-length mirror and are indicated in Fig. I-3 by an X near the data for each mirror. These approximate calculations show that the residence times are within a factor-of-3 of the observed breakdown times. Similar time-to-breakdown data for 6-, 10-, and 30-μm-diameter glass fibers show the same trend at slightly higher laser intensities. The scatter in these data was somewhat greater than that evident in Fig. I-3 and may have been due to large (~10 μm) particulates observed adhering to the fibers in photomicrographs.

The peak attenuation of the laser radiation in the breakdown plasma initiated on 100-μm-diameter glass fibers is shown in Fig. I-4 as a function of laser intensity. The solid circle denotes the threshold intensity. These peak absorption measurements show that the plasma becomes opaque to 10.6-μm radiation for only a factor-of-3 increase of laser intensity over threshold. The subsequent recovery of transmission through the plasma may be due to plasma expansion out of the depth of focus of the mirror into a region of lower laser intensity. In a few cases, the dynamics of the plasma expansion were photographed with a high-speed framing camera. Some results from these photographs are shown in Figs. I-5 and I-6 where the axial and lateral extent of the plasma are plotted as functions of time. The occurrence of a breakdown near the end of a laser pulse is shown in Fig. I-5 where the plasma expansion ended with the laser pulse. The occurrence of breakdown early in a laser pulse is shown in Fig. I-6 where the laser pulse continued for about 15 μsec after the plasma expansion had slowed considerably. These results indicate that the plasma absorbed much less laser energy after 10 μsec of expansion. The plasma velocity for these runs ranged from $6 \times 10^4$ to $10^5$ cm/sec.

The simple analysis of an expanding spherical blast wave due to Chernyi[6] may be extended to yield the following shock-wave trajectory for the case of time-dependent energy deposition:

$$R \sim t^{(\alpha+2)/5} \tag{I-2}$$

where $\alpha$ is defined by

$$\int_0^t q_a(t)\, dt \sim t^{\alpha} \quad . \tag{I-3}$$

Here R is the shock-wave radius, t is time, and $q_a(t)$ is the laser intensity absorbed by the breakdown. For instantaneous energy deposition, $\alpha = 0$ and $R \sim t^{2/5}$ which is the blast-wave solution. For the two shots shown in Figs. I-5 and I-6, the transmitted laser pulse indicates that the absorbed intensity increased linearly with time; in this case, $\alpha = 2$ and $R \sim t^{4/5}$. The data in Figs. I-5 and I-6 indicate that the slope varies from 0.75 to 0.96 and agrees well with the slope of 0.8 derived above.

J. E. Lowder
H. Kleiman

2. Particle-Induced Breakdown in Aerosol

The experimental measurements of breakdown threshold vs aerosol particle size, which were reported in the previous Optics Research Report (see p. 19 in Ref. 1), have been extended to a variety of materials. These data are shown in Fig. I-7. Note that these data were obtained with a short (200-nsec) TEA laser pulse. Thresholds for particles smaller than ≈20 μm were obtained by using a statistical method: filling the focal volume of the laser with a large number

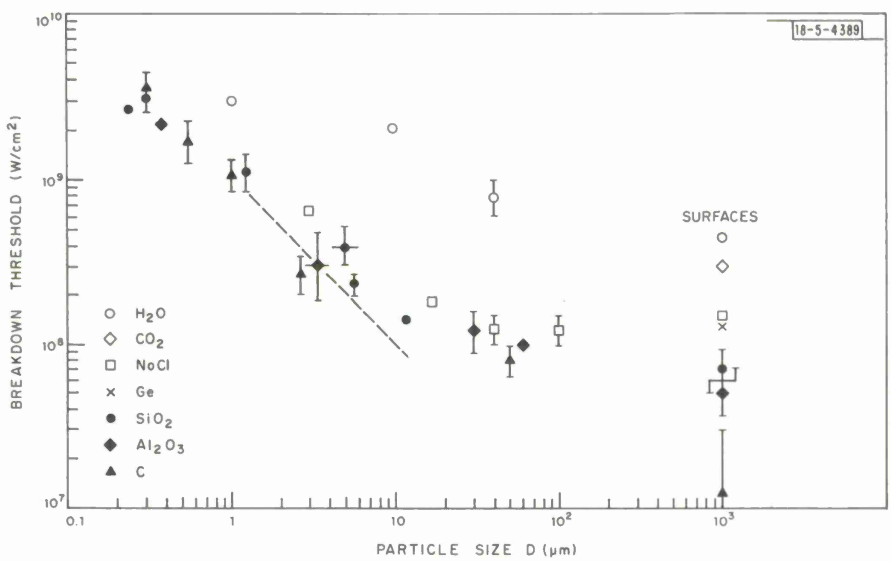


Fig. I-7. Breakdown threshold vs particle size for various materials. Thresholds at 1 mm are for solid surfaces in 1-mm beam.

of particles with a known size distribution. Particles larger than about 25 μm were dropped individually into the laser beam. The dashed line corresponds to laboratory air particles which were of unknown composition. The water aerosol was generated with a household cool-mist vaporizer. Data at 1 mm correspond to the thresholds for solid surfaces in a 1-mm beam. For some solid surfaces it was difficult to differentiate between surface vapor incandescence and air breakdown. This accounts for the error bars on these points. The $H_2O$ and $CO_2$ surface data were obtained with ice and dry ice.

The data for aerosols indicate that the threshold is fairly insensitive to material parameters with the one exception of water. For surfaces there is an order-of-magnitude variation in threshold. Note that the order of the thresholds for surfaces is generally maintained for particles.

The high threshold for water can be attributed to its low-vapor temperature – an order-of-magnitude lower than most materials. A high-vapor temperature lowers the threshold in two ways: first the initial degree of ionization in the vapor is higher and therefore the required number of generations to ionize the vapor is less. This goes as $k \approx x/T_v - b$, where x is the ionization potential, and b is a constant of the material with $b \sim 10^{-1}$. The second effect is that a higher $T_v$ drives a stronger shock wave in air, thus lowering the threshold for breakdown in the shock heated layer.

D. E. Lencioni

3. Aerosol Clearing with a 10.6-μm Precursor Pulse

The breakdown threshold of a high-intensity pulse in aerosol-laden air was increased by the application of a low-intensity precursor pulse of sufficient energy to remove particles from the beam. This occurred by either vaporizing, fragmenting, or jetting particles out of the beam. Also, the breakdown threshold for longer pulses ($\tau \gtrsim 1$ μsec) and 50-μm particles was 100 to 300 times lower than the clean-air case, in agreement with other reported results (see Sec. 1 above and Ref. 7).

The laser pulses were provided by two separate lasers. An E-beam $CO_2$ laser (see Ref. 4), with 10 J in a pulse time from 25 to 80 μsec, was used for the precursor pulse. A TEA $CO_2$ laser, with a peak power of 10 MW in a pulse time $\tau \approx 200$ nsec, was used for the high-intensity pulse. The second pulse was delayed a time $\tau$, which was variable from 0 to 0.1 sec. Two techniques were used in these experiments. In the first, a known distribution of small particles was contained in the focal volume of the beam. Aerosols up to 5 μm in diameter were studied in this way. The experimental arrangement is shown in Fig. I-8. The two beams were brought

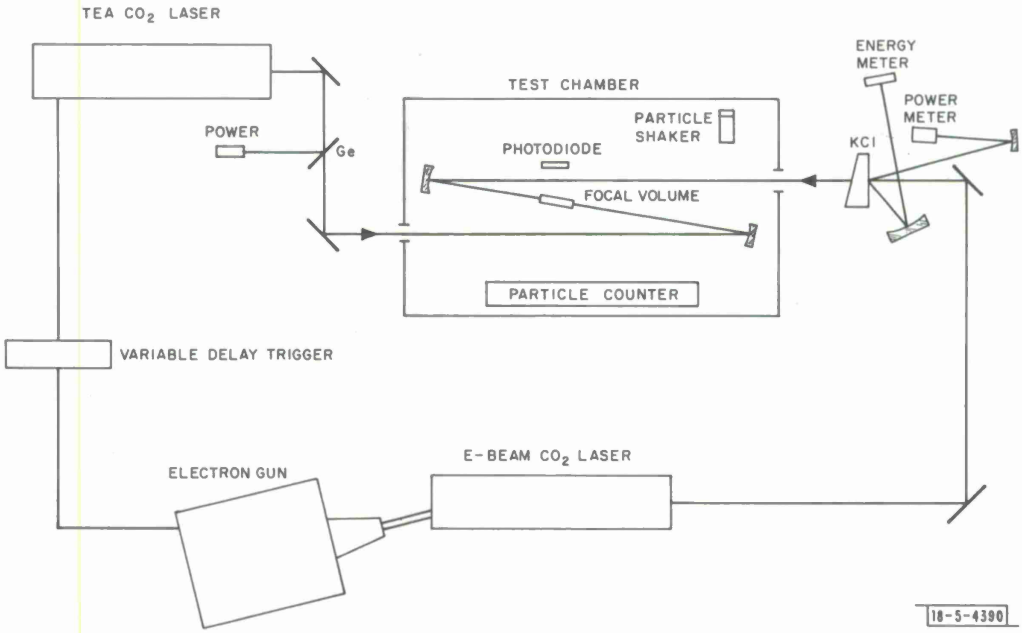


Fig. I-8. Schematic of apparatus used in double-pulse experiment. TEA laser was fired a time $\tau$ after E-beam laser.

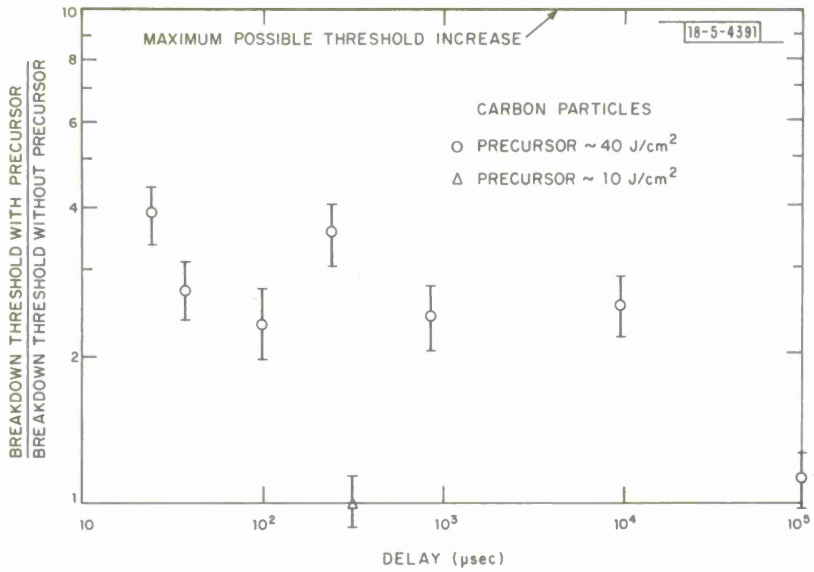


Fig. I-9. Relative threshold with and without precursor as a function of delay time for carbon aerosol.

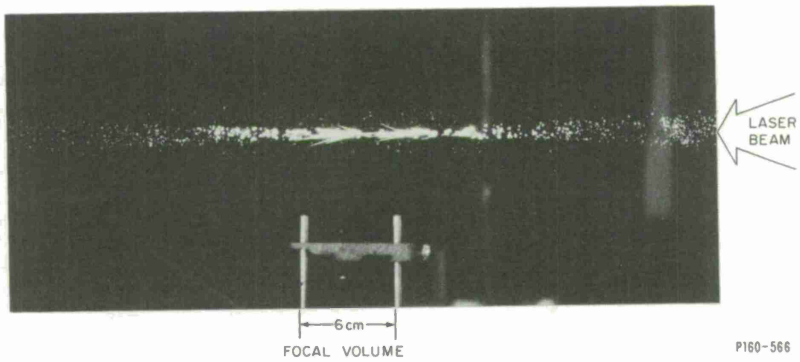


Fig. I-10. Effect of precursor pulse on carbon dust.

together from opposite directions so that the focal volume of the high-power pulse could be completely contained in that of the precursor. For this geometry, the precursor had a beam size of 3.5 mm and a depth of focus of 8 cm. A steady-state dust distribution was generated in the test box with a particle shaker and a small fan. The dust distribution was monitored with a Royco counter No. 225 and a Northern pulse-height analyzer No. NS-633.

Once a steady-state dust distribution was obtained in the test chamber, the breakdown threshold for the probe pulse alone was determined by attenuating with polyethylene sheets until breakdown was obtained on approximately 50 percent of the shots. The breakdown threshold was then determined for the combination precursor and probe pulse in the same manner. The threshold ratios for carbon dust are shown in Fig. I-9 as a function of the delay time between the end of the precursor and the beginning of the probe pulse. This dust distribution was such that the largest particle statistically predicted to be in the pulse laser focal volume was 4 μm.

These data indicate that the threshold was raised by factors of 2 to 4 for delay times up to 10 msec. The precursor pulse had no effect at delay times longer than 0.1 sec. This is consistent with particle velocities in the vicinity of the focal volume of about 2 cm/sec. It should also be noted that when the energy density of the precursor pulse was reduced by a factor-of-4 with a fine perforated screen, no threshold increase was observed (see Fig. I-9). An open-shutter photograph of the effect of the precursor pulse is shown in Fig. I-10. The streaks visible in the focal volume are due to the jetting action resulting from vaporizing particles on one side.

In the second technique, single particles 50 ± 10 μm in diameter were studied. These were dropped into the focal volume and detected by light scattered from a HeNe laser beam. This triggered the following sequence of events: a nanolight to obtain back-lighted photographs of the particles, the precursor pulse, and the probe pulse. The threshold was measured with and without the precursor. The carbon particles were observed to jet out of the focal volume and travel from 10 to 20 cm. An open-shutter photograph of a shot in which two carbon particles were in the focal volume is shown in Fig. I-11.

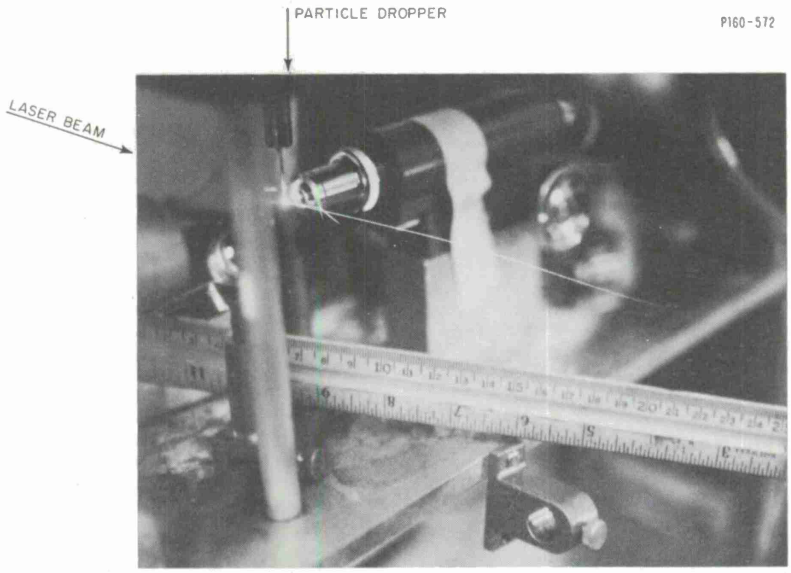


Fig. I-11. Jetting of single 50-μm carbon particle caused by precursor pulse.

The particles are heated to incandescence by the laser beam. One particle breaks into two pieces after hitting the microscope objective, while the other particle follows a curved path and exhibits a luminous intensity modulation produced by a spinning particle with one side incandescent. The short-pulse breakdown thresholds for these particles were found to be near $10^8$ W/cm$^2$. The precursor pulse raised the breakdown thresholds by factors of 19 and 11 for the carbon and alumina particles, respectively. The resulting breakdown threshold was about $2 \times 10^9$ W/cm$^2$, or just below the clean-air breakdown threshold. The long-pulse breakdown threshold for these particles was found to be approximately $2 \times 10^7$ W/cm$^2$, with time to breakdown varying from 1 to 15 μsec. These results are indicated by the arrows in Fig. I-13 of Sec. I-B-5 below.

We conclude from these results that the most likely mechanism for the observed threshold raising is jetting of particles out of the focal volume. Particles of 4-μm diameter and smaller may be vaporized and/or fragmented, but there is no direct evidence of the extent of these mechanisms. The details of the jetting process are described in Sec. 4 below.

D. E. Lencioni
J. E. Lowder

4. Momentum Transfer to Small Particles Irradiated by a Laser

As discussed in the previous section, glowing carbon particles were observed to jet out of the focal volume and travel from 10 to 20 cm in the general direction of the laser pulse. Occasionally, particles were observed to leave the focal volume at nearly 90° to the laser axis. The jetting action was caused by the laser beam vaporizing one side of the particle and imparting considerable momentum to it. The direction taken by any given particle is determined by its shape, since the resultant force is produced by vaporization and is normal to the local irradiated surface. The particle velocities were measured by viewing the glowing particle with a photomultiplier through an array of slits. The particle deceleration in air after an impulsive start is given by

$$m \frac{dv}{dt} = -\frac{1}{2} \rho_o A v^2 \tag{I-4}$$

where m is the particle mass, v is the velocity, $\rho_o$ is the density of air, A is the cross-sectional area of the particle, and the drag coefficient has been set equal to 1. This expression may be integrated to give

$$\ln v = \ln v_1 - \left(\frac{\rho_o}{m}\right) X \tag{I-5}$$

where X is the distance from the point of impulsive start.

A plot of ln v as a function of X is shown in Fig. I-12 for one shot. Here we note that the data are quite linear and yield a slope ($\rho_o$/m) of 0.16 cm$^{-1}$. The calculated value of a 50-μm-diameter particle with a density of 2.25 g/cm$^3$ is 0.08 cm$^{-1}$ and indicates that the drag coefficient is 2. Extrapolation of the data in Fig. I-12 yields an initial velocity of $6.2 \times 10^4$ cm/sec.

Since the absolute distance to the focal volume was uncertain on most of the shots, the initial velocities were found with the equation

$$v_1 = \frac{\bar{v}}{1 - \left(\frac{\rho_o}{m}\right) \bar{v}t} \tag{I-6}$$

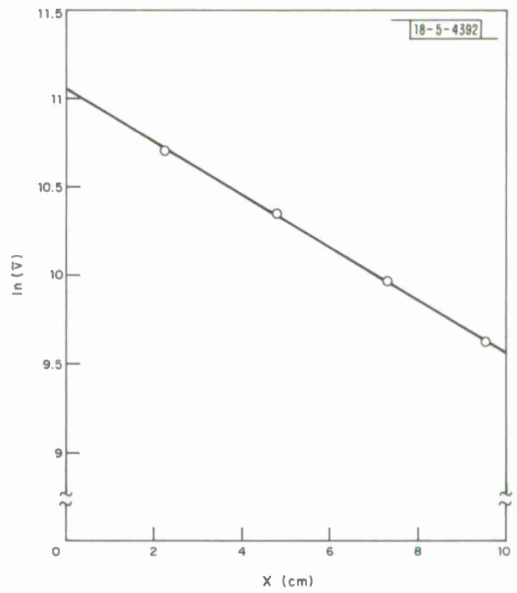


Fig. I-12. Logarithm of speed for jetting particle as function of position. Straight line implies drag force proportional to $v^2$.

which also results from integration of Eq. (I-4). Here, $\overline{v}$ is the average velocity measured at time t. The initial velocities ranged from $5.4 \times 10^4$ to $9.5 \times 10^4$ cm/sec for corresponding laser intensities of $1 \times 10^7$ and $2.4 \times 10^7$ W/cm$^2$. The average velocity was $7 \times 10^4$ cm/sec for an average intensity of $2 \times 10^7$ W/cm$^2$. At this velocity, a particle would remain in the depth of focus for about 13 μsec, or for about half the duration of the laser pulse. These results yield a coupling coefficient (I/E) of approximately 2. I/E is defined as the impulse (dyne-sec) imparted to the particle per joule of incident laser energy.

I/E may be estimated with the assumption of steady-state vaporization during the time the particle is in the depth of focus. The time to reach steady-state vaporization is given by[8]

$$t \simeq \kappa\left(\frac{\rho L}{q}\right)^2 \tag{I-7}$$

where $\kappa$ is the thermal diffusivity, $\rho$ is the density, L is the heat of vaporization, and q is the laser intensity. This time is 0.5 μsec for $q = 2 \times 10^7$ W/cm$^2$, $\rho = 2.25$ g/cm$^3$, and $L = 6 \times 10^4$ J/g. The total impulse transferred to a particle is given by

$$I = \int_0^{\tau} \dot{m} v(t)\, dt \tag{I-8}$$

where $\dot{m}$ is the mass loss rate, and v is the mass velocity. For steady-state vaporization, Eq. (I-8) becomes

$$I = \dot{m} v \tau \tag{I-9}$$

where $\dot{m}$ is given by qA/L. Equation (I-9) becomes

$$I/E = \frac{\overline{v}}{L} \tag{I-10}$$

by noting $E = qA\tau$ and $\tau \gg 0.5$ μsec. The mass velocity is given approximately by the average molecular velocity at the vaporization temperature

$$I/E = \frac{1.5 \times 10^4}{L} \sqrt{\frac{T_v}{M}} \tag{I-11}$$

where M is the molecular weight of the vapor. With the assumption of a vaporization temperature of 4000°K and a diatomic carbon vapor,[9] Eq. (I-11) yields an I/E of 3. This value must be considered a rough estimate since the actual composition of the carbon vapor is unknown and undoubtedly contains a significant amount of carbon chain molecules.[9] These experimental and theoretical I/Es agree well with the measurements of Gregg and Thomas[10] made in vacuum with large graphite targets irradiated with a ruby laser.

The maximum velocity obtainable in air at 1 atm can be found by equating the driving force to the drag force:

$$\frac{d}{dt} \left[\left(\frac{I}{E}\right) qAt\right] = \rho_o A v_{max}^2 \tag{I-12}$$

or

$$v_{max} = \sqrt{(I/E)\, q/\rho_o} \quad . \tag{I-13}$$

For this experiment, we have $v_{max} \simeq 2 \times 10^5$ cm/sec or only a factor-of-3 above the measured velocities. Note that this result is independent of particle size and only a weak function of particle material through (I/E). The time required to accelerate particles to the observed velocities is given by

$$t = \frac{mv}{(I/E)\, qA} \quad . \tag{I-14}$$

For $q = 2 \times 10^7$ W/cm$^2$ and I/E = 2 dyne-sec/J, a 50-μm carbon particle is accelerated to a velocity of $7 \times 10^4$ cm/sec in 13 μsec. The distance traveled in this time is approximately half the depth of focus as mentioned previously. These calculations are consistent with the observations and show that the measured velocities were limited by the finite depth of focus to about a factor-of-3 below the theoretical maximum.

J. E. Lowder
D. E. Lencioni

5. Characterization of Breakdown Data

The experimental data for 10.6-μm breakdown in air which has been reported recently can be characterized fairly well in terms of the breakdown threshold, the pulse length (or time to breakdown), and the particle size which triggers the breakdown. This is shown in Fig. I-13 where the data come from three sources: United Aircraft Research Laboratories,[11] Avco-Everett Research Laboratories,[12] and Secs. B-1, -2 and -3 above.

The data at 200 nsec, which were described in the previous section, show how the threshold is lower for larger particles but approaches a limit at slightly less than $10^8$ W/cm$^2$. For longer pulses, however, these large particles can cause breakdown at even lower thresholds. Very little data have been taken for long pulse times and small particles. In fact, only lower limits have been obtained (e.g., the open square in Fig. I-13) because of the need for a high-energy pulse. Note that the UAC data were taken with no knowledge of the particle distribution; however, the indicated particle size is reasonable for typical laboratory-air conditions.

D. E. Lencioni

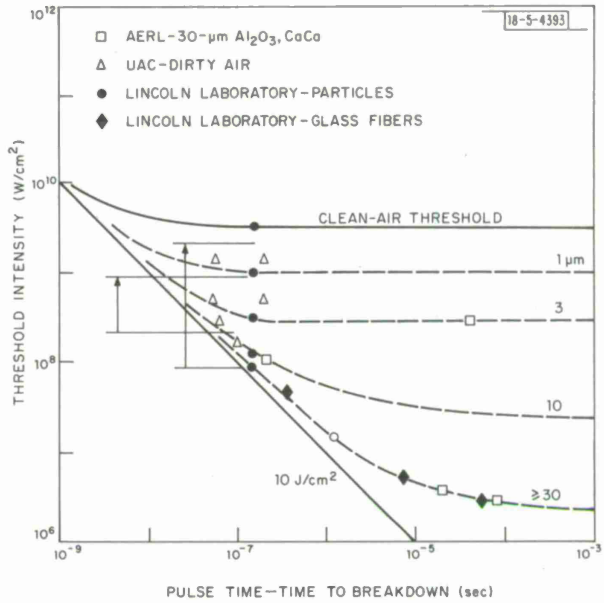


Fig. I-13. Characterization of breakdown threshold vs pulse length according to particle size that triggered breakdown. [Clean-air threshold plot from G. H. Canavan, W. A. Proctor, P. E. Nielsen and S. D. Rockwood, IEEE J. Quantum Electron. QE-8, 564 (1972).]

## C. LASER DEVICE TECHNOLOGY

The 500-J E-beam-excited laser oscillator has become operational producing a near-diffraction-limited beam and energies measured in excess of 700 J. Initial measurements have been made on the beam characteristics, and experiments have been initiated using the output beam. A study and experiments have been completed for shaping the pulse in time by both internal modulator control and by external means.

A small-scale photoionization laser has been successfully demonstrated, and work is presently under way for scaling this device to a large laser.

Power amplification of repetitive pulses on a large scale with maintenance of good beam and spectral quality has been studied theoretically.

### 1. 500-J E-Beam-Excited Laser

The Lincoln Laboratory 500-J E-beam-excited laser first operated successfully in August and has demonstrated a capability for outputs in excess of 700 J. Performance of the laser has been in satisfactory agreement with predictions, and the device is presently in active use in the surface effects and propagation programs.

A series of tests designed to optimize the energy output and beam quality and to determine the sensitivity of the device to mirror alignment and quality has been planned and will be interspersed with the use of the device as a tool for the various experimental programs.

A. J. Morency

### 2. Optical Output Characteristics of 500-J Pulsed Laser

The Lincoln Laboratory pulsed 10.6-μm laser has been described earlier (see Ref. 1, p. 37). The output beam near- and far-field distributions, temporal pulse shape, and output energy have been measured. To date, definitive diagnostics are incomplete, but on the basis of the multiple-burn-pattern technique first used by Marquet,[13] the laser has produced several hundred joules of focusable energy in a nearly-diffraction-limited spot. The highest energy output to date is

760 ± 75 J. More-precise and definitive measurements will be completed for a typical range of operating parameters in conjunction with dirty-air breakdown and surface interaction experiments that are now under way.

The output beam from the laser is typically 20 × 15 cm with a round, square, or rectangular obscuration caused by the feedback mirror. The various sizes and shapes are being used to determine empirically which is the best cavity configuration for beam brightness, maximum energy, or has the best focal-spot geometry for interaction studies. These optimization experiments are being interwoven with interaction studies to check the theoretical estimates of output beam characteristics with the various cavity configurations (see Ref. 1, p. 39). Figure I-14 is a typical example of the near-field output burn pattern from a cavity with 60-percent outcoupling and with a rectangular feedback mirror.

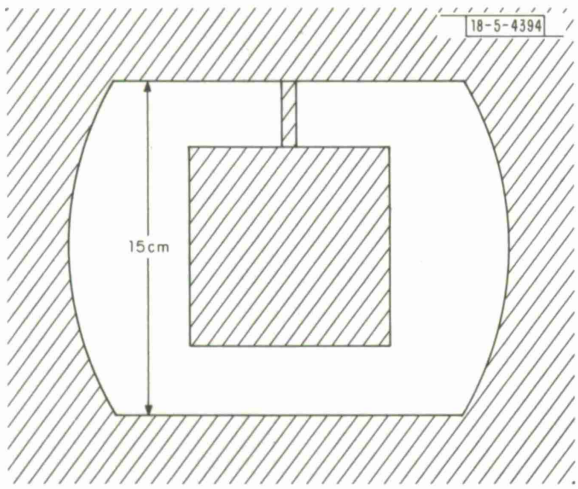


Fig. I-14. Near-field burn pattern from Lincoln Laboratory E-beam laser.

Figure I-15 is a schematic of the high-energy-laser laboratory illustrating the location of the laser, beam-directing optics, and diagnostic apparatus. Initial operation is with 25-m focusing optics, but optical paths of as long as 100 m are readily available. Diagnostic procedures are similar to those already demonstrated in the experiments performed with Avco-Everett Research Laboratory's "Big Bang" laser.[14] The beam leaving the laser is incident on a 30-cm-diameter, 25-m focal-length spherical mirror $M_1$ that directs the beam to a turning flat $M_2$ where it is reflected through a 90-percent transmittance diagnostic grating G to the focal volume located over a two-dimensional optical bench containing experimental and diagnostic instrumentation. The energy in the focal spot is attenuated to 81 percent of the total focusable energy by the diagnostic grating but is otherwise unperturbed. This high-energy focused beam is used for experiments. Of the other 19 percent, 9.5 percent are reflected backward and lost, while the remaining 9.5 percent fall into symmetric sets of monochromatic side orders that are used for beam diagnostics. With the grating geometry chosen, the energy in the first 7 side orders ranges from about 1 to 0.2 percent of the high-energy zero-order beam. Typical instrumentation in the side orders are calorimeters, fast-response detectors, and thermally sensitive burn-pattern materials which measure power, total energy, energy density, and the focal-spot distribution. With adequate sampling and a properly chosen grating and propagation geometry, the spatial energy distribution in each side order can be exactly related to the primary high-energy focal spot.

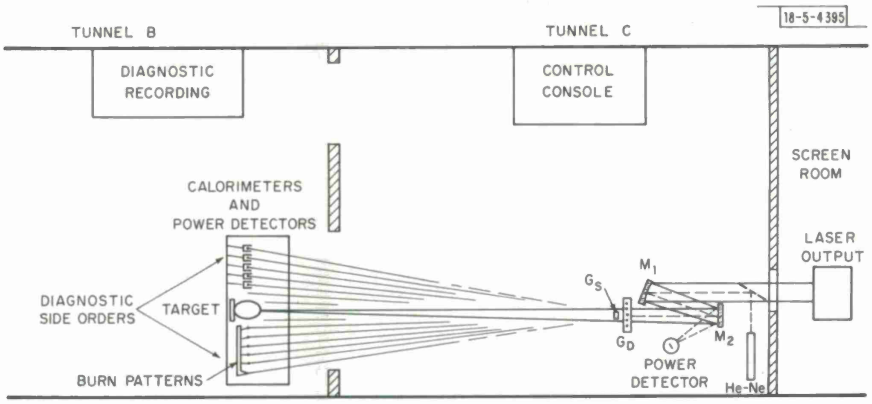


Fig. I-15. Schematic of high-energy-laser laboratory.

To calibrate the diagnostic grating, a highly reflective, high-dispersion, low-transmittance grating is placed between the diagnostic grating and focal volume so as to intercept only the zero order after the diagnostic orders have been dispersed. This technique is illustrated in Fig. I-16. The zero-order energy reaching the focal plane is preferentially attenuated by the square of the geometrical or amplitude transmittance of the attenuation grating to a level appropriate for commercially available calibrated calorimeters. The diagnostic side orders which are not affected by the zero-order attenuation procedure are measured with individual relative calorimeters which can, if calibrated, yield the absolute energy distribution in the grating orders for the particular laser, grating, and propagation geometry.

To place the various detectors in the diagnostic orders precisely, a grating was fabricated that places visible side orders generated by a carefully aligned He-Ne laser in exactly the same position as the 10.6-μm orders. This is illustrated in Fig. I-15.

Figure I-17 is the temporal output of the laser as measured with a laboratory-fabricated photon drag germanium detector placed in the first diagnostic side order.[15] Energy measured on this shot in two calibrated grating orders was 760 ± 100 J. Figure I-18(a) is a set of burn patterns of the grating orders on one side. Knowing the threshold for discoloration of the particular material and the distribution of energy in the grating orders, the spatial distribution of energy in the focal spot can be estimated as is illustrated in Fig. I-18(b). When calibrated scanning calorimeters are placed in a number of grating orders, the total energy present in the focal spot can be measured definitively with a single shot. This latter operation is scheduled for the near future.

R. W. O'Neil J. E. Lowder
H. Kleiman D. E. Lencioni

3. E-Beam Laser Kinetics

The kinetics program was refined to include a finite vibrational equilibration time for the $\nu_1$ vibrational mode of $CO_2$. If the assumption of instantaneous vibrational equilibration were inadequate, it would be most seriously in error for the $\nu_1$ mode where there is no vibrational dipole moment and thermalizing interactions are relatively weak. The addition of the appropriate equation, however, led to no significant changes in the gains, pulse energies, and pulse lengths, and thus confirmed our confidence in the five-temperature model.

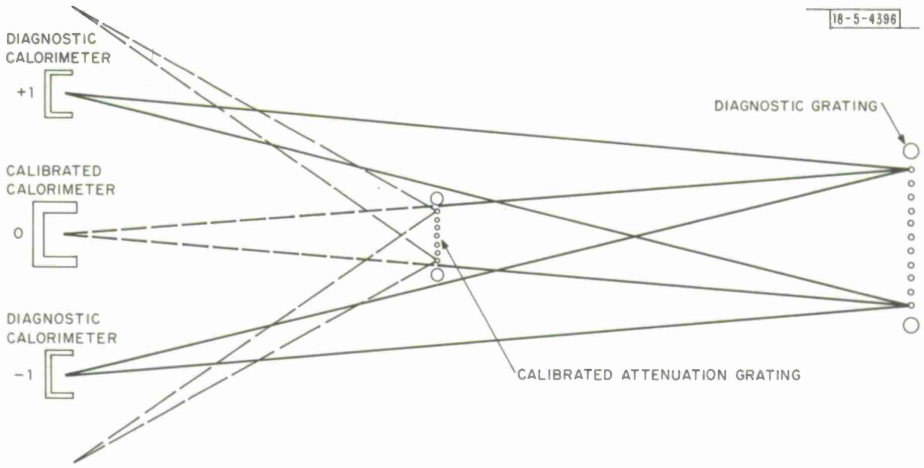


Fig. I-16. Schematic of grating calibration procedure.

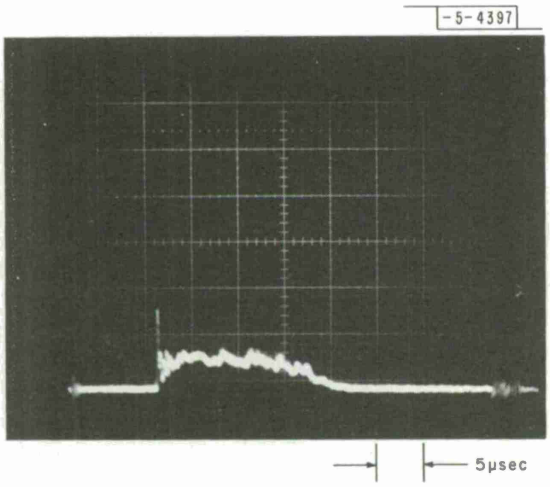


Fig. I-17. Temporal output of E-beam laser as measured with photon drag detector.

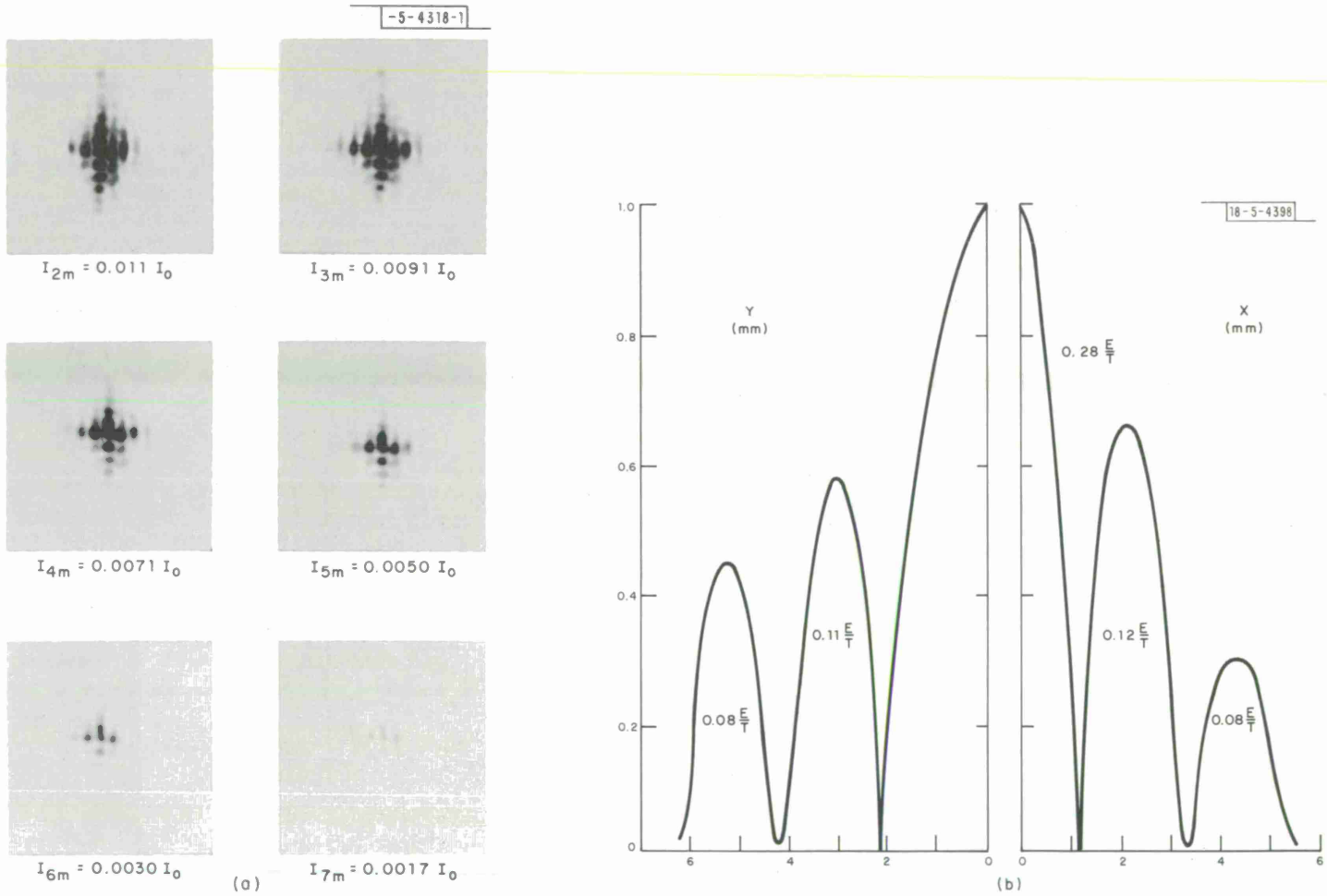


Fig. I-18. Beam-profile measurement. (a) Burn patterns from six grating orders; (b) relative irradiance distribution derived from ideal grating distribution.

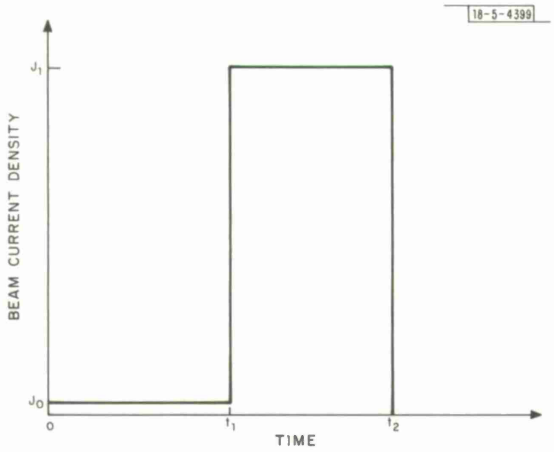


Fig. I-19. Proposed E-beam pulse shape for elimination of initial spike by minimizing initial inversion when laser breaks into oscillation ($t_1$ = time at which oscillation commences).

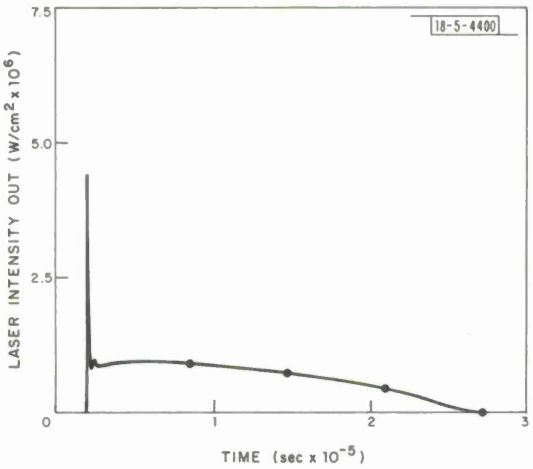


Fig. I-20. Computer-generated laser pulse shape for $J_0 = J_1 = 20$ mA/cm$^2$.

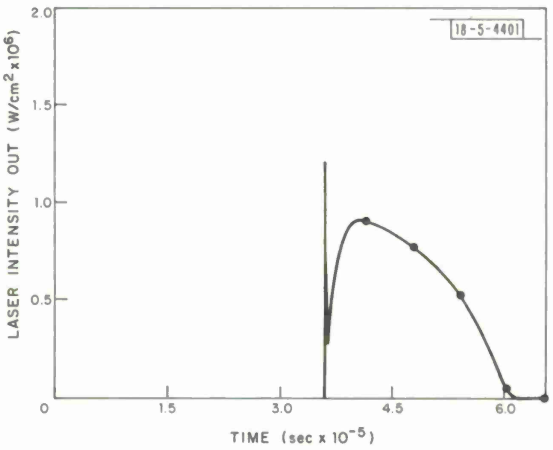


Fig. I-21. Computer-generated laser pulse shape for $J_0 = 0.05$ and $J_1 = 20$ mA/cm$^2$.

The rate equations were further corrected to take proper account of the photon decay time in the laser cavity, and this correction increased the computed width of the initial spike from ~50 to ~200 nsec, in agreement with experimental observation.

Computations were also performed to test theoretically a proposal for eliminating this spike. This is a desirable objective inasmuch as the high peak intensity can lead to air breakdown.

The spike results from the very high population inversion density which exists as the laser oscillation is building up. This is due to the fact that, at this time, the flux is not sufficient to bring the gain down to its threshold value, where it just balances the cavity losses. Therefore, in order to lower the intensity of this spike, one might attempt to lower the rate at which the inversion is building up at the onset of oscillation.

One scheme for achieving this for E-beam lasers is indicated in Fig. I-19. In this approach, the primary E-beam current is maintained at a low value until lasing begins, at which time the full desired current is switched on. The effectiveness of this technique is indicated by Figs. I-20 and I-21 which show computer-generated pulse shapes. In Fig. I-20, the full beam current density of 20 $mA/cm^2$ is used throughout, while in Fig. I-21 the current density is initially 0.05 $mA/cm^2$. Note that the ratio of peak-to-tail pulse height drops by approximately a factor of 3. The low initial current, however, also causes a long delay before lasing.

It is clear that this method requires a technique of rapidly (<1 μsec) sensing the onset of laser action and delivering this information to the E-beam modulator. This, of course, may be accomplished by sampling a small portion of the laser output, but it is probably desirable to interfere with the beam as little as possible. One might also take advantage of the change in impedance characteristics of the laser medium, but it appears these changes are too insensitive in their RF noisy environment.

One technique that appears promising is that of monitoring the spontaneous 4.3-μm emission through a viewing port in the laser chamber. As lasing begins, there is a marked decrease in the number of vibrationally excited $CO_2$ molecules, and hence a corresponding decrease in the spontaneous emission rate. The change in current through a photoconductive detector could then be used to switch the modulator. Preliminary calculations indicate that there is sufficient spontaneous emission at the onset of oscillation to make this technique feasible.

During this reporting period, solutions of the Boltzmann transport equation for several gas mixtures were obtained from W. Nighan of United Aircraft Research Laboratories and were reduced to a form compatible with our kinetics code. These solutions, which give the electron energy distribution function, enable us to add a range of gas mixtures as a variable parameter to our calculations.

S. Marcus
D. M. Zanni*

4. E-Beam Laser-Pulse Shaping

Experimental work was completed on the use of saturable absorbing gases for externally shaping $CO_2$ laser pulses, and a paper describing the results has been accepted for publication in the Journal of Applied Physics.[16] In summary, absorbers were used to generate ramp-shaped pulses or to eliminate or accentuate the initial spike as desired. In addition, a simple theoretical description of the observed phenomena was developed.

---

* Philco Corporation.

Preliminary attempts were also made to operate the Febetron-excited laser[4] in two other modes (short-pulse and passively Q-switched) besides the normal long-pulse (20- to 80-μsec) mode. In short-pulse operation, the E-beam is used to create a pre-ionization for a uniform avalanche discharge. In this mode, a pulsed voltage higher than the breakdown voltage of the laser medium is applied to the electrodes, rapidly dumping the entire stored energy into the gas. The circuit shown schematically in Fig. I-22 was used for this purpose.

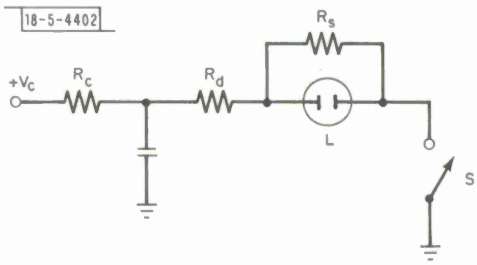


Fig. I-22. Schematic of laser pulsing circuit. L is laser electrodes, S is triggered spark gap, $V_c$ and $R_c$ are charging voltage and resistance, $R_d$ is damping resistance, and $R_s$ is laser shunt release.

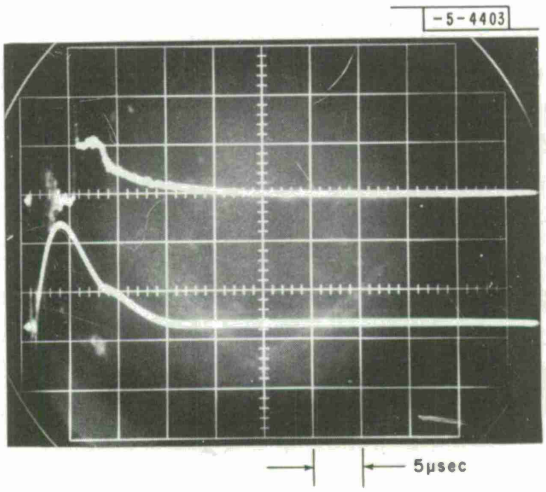


Fig. I-23. Operation of Febetron laser in short-pulse mode. Upper trace is laser pulse, lower trace is current pulse. Circuit parameters are $V_c$ = 26 kV, $R_d$ = 10 ohms, and $R_s$ = 23.5 ohms.

Figure I-23 shows the laser pulse shape obtained with this technique as well as the current pulse shape. The peak power of this pulse (neglecting the initial spike) is ~700 kW, somewhat higher than is obtained in the long-pulse mode. Our data indicate that further increases can be expected if we deliver the electrical energy to the gas even faster. This can be accomplished by increasing the charging voltage while reducing the storage capacitance. We plan to do this at the earliest opportunity.

In our preliminary efforts at passively Q-switching the Febetron-excited laser, attempts to Q-switch with $BCl_3$ have been unsuccessful as we were unable to obtain sufficient absorption using the 10-inch absorption cell at our disposal. However, marginal results were achieved with $SF_6$ as the absorber. The problem with $SF_6$ is that intra-cavity wavelength selectivity, such as with a diffraction grating, is required for Q-switching. This makes cavity alignment extremely difficult for our single-pulse system. We are presently planning to utilize a longer absorption cell so that we may use $BCl_3$ and thus eliminate the need for a diffraction grating.

H. Kleiman R. W. O'Neil
S. Marcus L. C. Pettingill

5. Observation of Laser Oscillation in a 1-atm $CO_2$-$N_2$-He Laser Pumped by an Electrically Heated Plasma Generated via Photoionization

In a previous publication,[17] the authors considered the possibility of producing large-volume plasmas via photoionization in high-pressure gas laser media of sufficient electron density to

sustain laser oscillation. Several general approaches were outlined. One requires that the host laser medium be seeded with the vapor of a low-ionization potential species. The concentration of the seed gas is kept low enough so that the penetration depth of photons which partake in the single- or multi-step ionization of the added species is larger than the dimensions of the plasma. This, together with the requirement that the relevant photon energies be sufficiently low to avoid absorption bands in the host laser medium, insures the production of a uniform plasma. Furthermore, the low photon energies permit the use of readily available UV windows. The resultant photoelectrons are then heated in an externally applied electric field to the optimum temperature for population inversion in the laser states.

We report here the first successful operation of a device embodying this concept. A 1-atm mixture of $CO_2$-$N_2$-He was chosen as the laser medium. To this was added a small quantity of the seed gas, tri-n-propylamine, $[CH_3(CH_2)_2]_3N$, having an ionization limit lying 7.23 eV above the ground state. An electric field was established between two parallel polished electrodes 20 cm long, 1 cm wide, and spaced by 1 cm, thereby defining the volume throughout which population inversion occurs. The ionizing photon flux was produced by two standard xenon flashlamps, employing quartz envelopes, flanking the electrodes as shown in Fig. I-24. The laser cell was provided with two 2-m radius-of-curvature internal mirrors, one gold coated and one 10-percent transmitting germanium, used for output coupling.

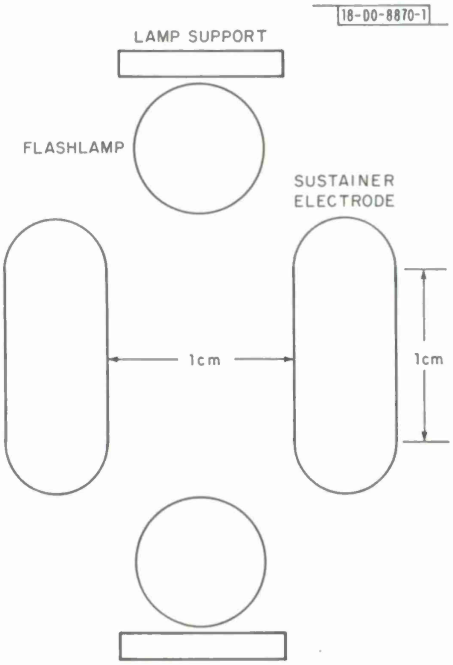


Fig. I-24. Laser lamp and electrode arrangement viewed parallel to optical axis.

Because of its low ionization potential, tri-n-propylamine can be ionized by UV with wavelength as long as 1715 Å in a single-step process. This fact made it an attractive candidate for seeding a $CO_2$-$N_2$-He laser where strong molecular absorption bands are encountered only for wavelengths shorter than 1600 Å. Prior to attempting to obtain laser oscillation, a series of experiments was conducted to study the photoionization of tri-n-propylamine. An electrode, lamp arrangement similar to that used for the laser and shown in Fig. I-24 was used. Nitrogen was flowed through the cell. A variable fraction of the $N_2$ flow could be bubbled through a vessel containing liquid tri-n-propylamine to permit control of the density of seed gas.

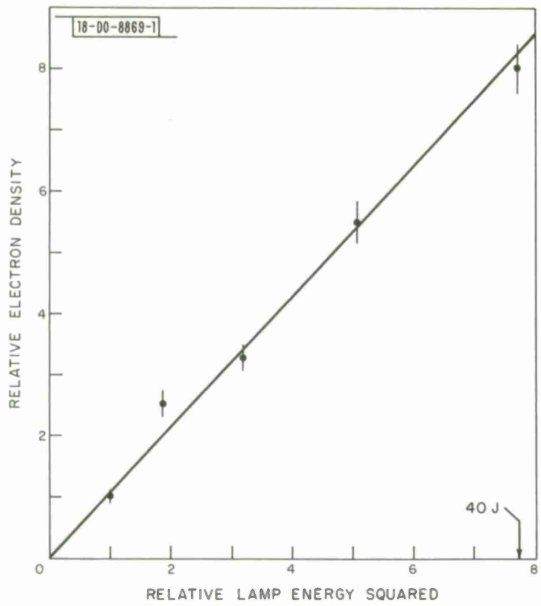


Fig. I-25. Photoelectron density vs square of flashlamp energy, both scaled in arbitrary units.

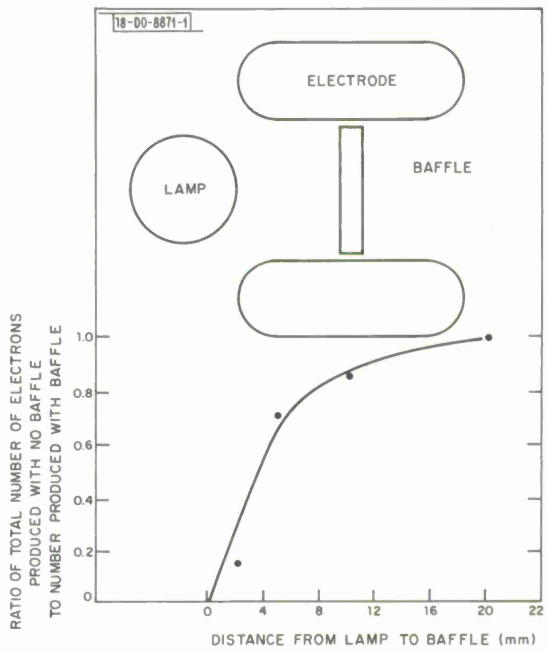


Fig. I-26. Normalized number of electrons produced vs lamp-baffle distance. Superimposed sketch of electrodes, lamp, and baffle is drawn to scale of abscissa.

In a typical experiment, a dynamic equilibrium pressure of 500-torr $N_2$ doped with approximately 0.5-torr tri-n-propylamine was established. The photoelectron current was monitored with a current transformer and displayed as one trace on a dual-beam oscilloscope. The flashlamp light pulse was monitored with a photomultiplier and displayed on the second oscilloscope trace. Typically, the light pulse was of 2-μsec duration. The photoelectron current lagged behind the light pulse by approximately 1 μsec, beginning just as the light pulse peaked and lasting somewhat longer than the light pulse. A plot of photoelectron current vs collector voltage was found to be linear for sufficiently low values of voltage, indicating that no electron avalanche was produced. All measurements were made with this in mind; accordingly, the collector current gave a direct measure of the photoelectron density. In the absence of tri-n-propylamine, no collector current could be discerned.

Figure I-25 is a plot of relative electron density vs the square of the flashlamp input energy over the range 0 to 40 J. Clearly, electron density is proportional to the square of the photon flux. This indicates that photoionization takes place by a two-step process and that the dominant electron-loss mechanism is either via attachment or diffusion, and not by recombination. The latter would imply an electron density proportional to the first power of the photon flux for a two-step process. The time delay between the initiation of the light pulse and the onset of a photocurrent is further evidence of a two-step process, 1 μsec being the time required to populate the intermediate states. Additional experimental evidence obtained in support of the two-step hypothesis is that photoionization was produced with the lamp external to the cell. Photons had to traverse a 5-mm air path to reach the tri-n-propylamine-doped $N_2$. Oxygen in the air absorbs strongly below 1715 Å and yet no change in photocurrent was observed when the air path was thoroughly flushed with $N_2$, indicating that photons less energetic than the ionization energy are primarily responsible for plasma production.

The spatial distribution of photoelectrons was probed by a simple technique. Only one of the lamps indicated in Fig. I-24 was fired. An opaque baffle was inserted between the electrodes running parallel to the lamp and perpendicular to the electrodes. By changing the distance from the lamp to the baffle, a variable volume element could be shielded from ionizing radiation. By noting the collector current for each of several baffle positions, the plot of Fig. I-26 was obtained which shows the normalized number of photoelectrons contained within a volume defined by the electrode separation, the lamp-to-baffle distance, and the electrode length. The shape of the curve indicates that electron density falls off with distance from the light source. This is reasonable and entirely attributable to the fact that no attempt has been made to collimate the light. The photon flux falls off inversely with distance; and because the electron production rate is proportional to light flux squared, the electron density should vary inversely with distance squared. Even so, it is apparent from Fig. I-26 that 25 percent of the electrons fall within the flat portion of the electrodes where they can contribute to the population inversion. Curves similar to that in Fig. I-26 were obtained for a very lean mixture of tri-n-propylamine and for one 30 times richer. The similarity of the results indicates that even for the rich mixture, the medium is optically thin to the ionizing radiation and that uniform excitation over very large volumes may be achieved by using a collimated light source.

A $CO_2$-$N_2$-He laser was constructed using the lamp and electrode arrangement shown in Fig. I-24. Two lamps were used to improve the uniformity of illumination between the electrodes. These lamps had envelopes of 9.5-mm o.d. and 1-mm-thick quartz, and an arc length of 30.5 cm. Because the collecting, or now more properly the sustainer, electrodes were 20 cm long, 5 cm

of arc length was masked on each end of the lamps to prevent plasma formation outside the region of the sustaining field. The lamp capacitor could be charged to a maximum of 30 kV which represents an energy storage of 225 J. The sustainer field was maintained nearly constant during the time of plasma formation and population inversion by a large, 8-μF capacitor wired across the sustainer electrodes and charged to the desired voltage. Both the lamps and electrodes were housed inside a 50.8-cm length of 10.16-cm i. d. pyrex pipe. Lucite end plates made a vacuum seal and provided support for the internal mirror mounts. Various gas mixtures were used, all with a total pressure of 760 torrs, and all were flowed slowly through the laser. In all cases, the laser gas was lightly doped with tri-n-propylamine; a very rough estimate of the partial pressure of seed gas is 0.25 torr.

Figure I-27 shows three simultaneous oscilloscope traces which display from top to bottom: the output of a photomultiplier monitoring the flashlamp output, the sustainer current, and the output of a liquid $N_2$-cooled GeAu detector monitoring the attenuated laser output. The timebase is 5 μsec/cm and the vertical scale of the sustainer current is 100 A/cm. The gas mixture used in this case was a 3:2:1 ratio of $He:N_2:CO_2$, and the lamp energy was approximately 200 J. Note the small delay of the sustainer current relative to the lamp pulse, as mentioned in the previous section.

The sustainer field was 4000 V/cm, corresponding to E/P = 5.3; from this and the known mobility of electrons,[18] we estimate the peak electron density. From Fig. I-27, the peak photoelectron current is 150 A of which 25 percent flow between the flat portions of the sustainer electrodes. This represents a current density, j, in the active region of 38 A/20 $cm^2$ = 1.9 A/$cm^2$. The drift velocity of electrons for this value of E/P is $v \cong 2.6 \times 10^6$ $cm^2$/sec. The peak electron density ($n_e$) is determined from: $j = en_e v_D$, where e is the electronic charge $1.6 \times 10^{-19}$ C, as $n_e = 5 \times 10^{12}/cm^3$.

The laser output energy was measured for various gas mixtures and sustainer fields with a calorimeter. Results are summarized in Fig. I-28. For each mixture, sustainer voltage was

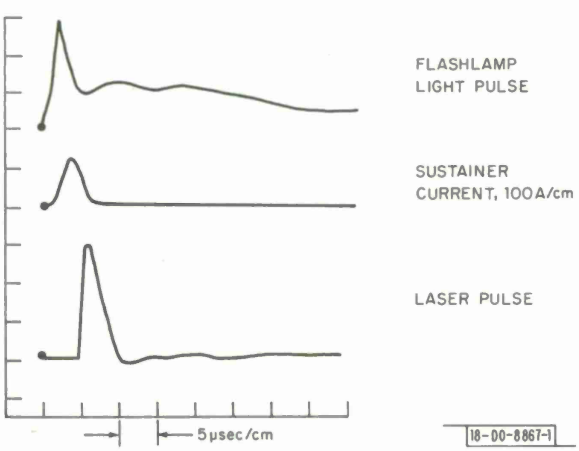


Fig. I-27. Flashlamp light pulse, sustainer current, and 10.6-μm laser pulse from lightly doped 3:2:1 ratio of $He:N_2:CO_2$, 1-atm mixture.

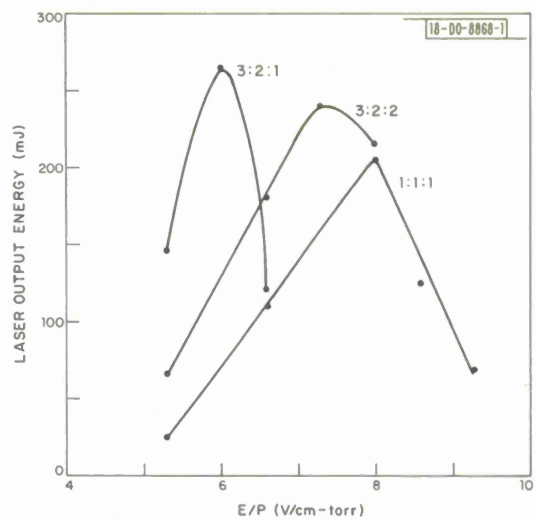


Fig. I-28. Laser output energy vs sustainer field strength divided by laser gas pressure. Ratios indicated denote gas mixture, $He:N_2:CO_2$.

varied from a low value corresponding to laser threshold to a high value corresponding to electrical breakdown in the gas prior to lamp firing. A clearly defined maximum in each curve demonstrates that the mean electron energy may be tuned to the optimum value for population inversion. This freedom had previously been available only in the rather elaborate E-beam, sustainer lasers of recent development.[19]

The maximum energy coupled out of this device was 300 mJ obtained from a 1:1:1 mixture very heavily doped with tri-n-propylamine. The heavy doping produced a peak electron density of $10^{13}/cm^3$ and a slight increase in laser energy at the expense of greatly reduced conversion efficiency of sustainer energy to infrared energy. This peak energy corresponds to an outcoupled energy density of 15 J/liter.

Spectroscopic analysis reveals that laser oscillation occurs on the P(20) transition for the 3:2:1 mixture. The small signal gain near 10.6 μm was measured in a lightly doped 3:2:1 mixture with E/P = 6. For this purpose, the internal mirrors were removed and replaced by NaCl Brewster angle windows. A small, 1/2 W, CW $CO_2$ laser oscillating on several high-gain P-branch transitions was aligned to direct its 10.6-μm beam along the optical axis of the device and then into a GeAu detector. As the amplifier was pulsed, the peak detector signal was noted and the ratio of this number to the signal obtained from the mechanically chopped CW laser gave the gain over the 20-cm-amplifier path as approximately 15 percent.

The device described here possesses the advantages of E-beam lasers: the freedom to optimize the mean electron energy; and the capability of producing large-volume, stable, uniform plasmas in high-pressure systems. However, it is inherently a much simpler device and therefore more reliable. Our approach circumvents the engineering difficulties associated with the production of large-area, high-current E-beams of hundred kilovolts energy. The photoionization technique lends itself naturally to the extension into the realm of very high-pressure gas lasers. To operate a large E-beam device at 10- or 20-atm pressure would require an electron gun engineered for 1 to 2 MV – a formidable task. The extension of our approach to very high-pressure systems is an elementary matter because, unlike the ionizing electrons of the E-beam, the penetration depth of ionizing photons is independent of the pressure of the host laser gas. Such a very high-pressure $CO_2$ laser would possess unique properties, among which are: very high-energy density and a totally pressure-broadened gain profile, making possible ultra-short, high-power, mode-locked pulses, as well as a broadly and continuously tunable coherent source.

The overall electrical efficiency of the initial device described herein is rather low for two reasons. The first is, of course, that no attempt has been made to collimate or direct the lamp light; much of it simply goes out the sides of the laser and is wasted. The second, more serious, deficiency is that only about 1 cm of the penetration depth of each ionizing photon is used to create electrons for laser excitation. We estimate the penetration depth to be at least on the order of a meter, and perhaps much greater. Both shortcomings may be overcome by judicious collimating and directing of the lamp light.

J. S. Levine
A. Javan

6. Large Photoionization Laser

With the successful demonstration of photoionization as a pumping mechanism for $N_2$-$CO_2$-He lasers by Javan and Levine,[17,20] it becomes desirable to demonstrate experimentally the scaling of this type of laser to a large-volume, high-energy-per-pulse device. Toward this end, an effort has been started with essentially three goals. The first of these is technology improvement: a search for other seed molecules with more desirable properties than tripropylamine, an

investigation of flashlamp design to optimize the pumping of the seed molecules with high efficiency, and a study of cavity-illumination techniques to optimize the photon uniformity.

Second, there is a small effort to demonstrate as soon as possible the production of large-energy pulses by converting the present 500-J E-beam-excited laser to a 500-J flashlamp-excited laser. Finally, we wish to optimize the design of a several-hundred-joules-per-pulse flashlamp-excited laser. The progress on these programs is discussed below.

a. Lamp-Emission Spectra

A test facility has been constructed for measuring lamp spectra so that optimization of the energy distribution can be achieved. A schematic of the facility is shown in Fig. I-29. An RCA S19(7200) photomultiplier (CsSb) is placed 2 inches from the lamp and measures a signal proportional to the total lamp flux from the center of the tube. A Pearson 110A current probe measures the time history of the lamp-driving current. The photon flux passes through a Heath Schlumberger 700 monochrometer (~250-μm slits for the spectrum corresponding to a resolution bandwidth of about 40 Å) to an EMI 9558QB (S20Q) photomultiplier attenuated also by internal filters in the monochrometer. Spectra are taken on a point-by-point basis and adjusted to the wideband peak flux. A sample measured spectrum of a 12-inch arc length xenon lamp driven by a 12-kV, 100-J supply in a 3-μsec pulse is shown in Fig. I-30. A variety of lamps with a range of driving circuits will be tested on this facility.

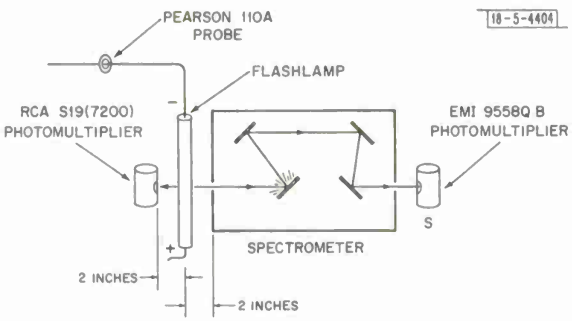


Fig. I-29. Schematic of lamp-emission spectroscopy measurements. One photomultiplier measures total intensity, one measures portion of spectrum through monochrometer, and probe measures total current through lamp.

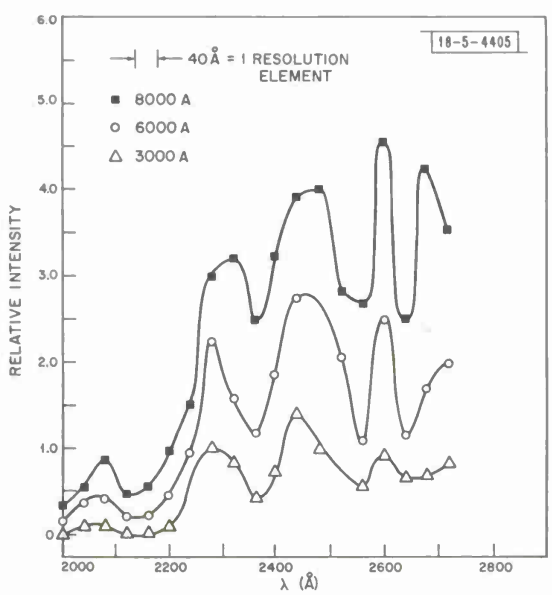


Fig. I-30. Typical flashlamp-emission spectrum from 2000 to 2720 Å. Taken on 12-inch arc length xenon flashlamp (7 J in 3 μsec) for three current densities.

b. Near-UV Spectroscopy

As part of the photoionization experiments, we have established test facilities to measure the absorption spectra of seed molecules. Thus, efficient usage of the photon pumping energy can be achieved.

Using a dual-beam Beckman DK-2A ratio recording spectrophotometer, measurements were made of tripropylamine, tributylamine, and tripentylamine in the spectral range from 1850 to 3600 Å. Static measurements were made on the vapor above the liquid, which had reached equilibrium with air in a suprasil test cell. These three organic compounds show respectively decreasing photoionization cross sections. Figures I-31(a) through (c) show the characteristic absorption spectra for the three compounds in 0.5-, 1-, and 5-cm cells, respectively, as well as the reference trace with empty cells. The vapor pressure of tripropylamine is 2.9 torrs at 20°C, and that of tributylamine is 2.6 torrs at 20°C. Using these values and assuming a value of 2.3 torrs for tripentylamine, we get respective peak absorption coefficients in the near-UV of 0.83 (at 2140 Å), 0.082 (at 2125 Å), and 0.062/cm-torr ($\lambda_{max}$ < 1850 Å).

We also observe the peak absorption shifts farther toward the UV as we change from tripropylamine to tributylamine to tripentylamine (therefore less efficiently using the flashlamp light with its peak at about 3000 Å), explaining the order of their reduced efficiency. The test facility will be used in the future for pre-sampling possible seed gases.

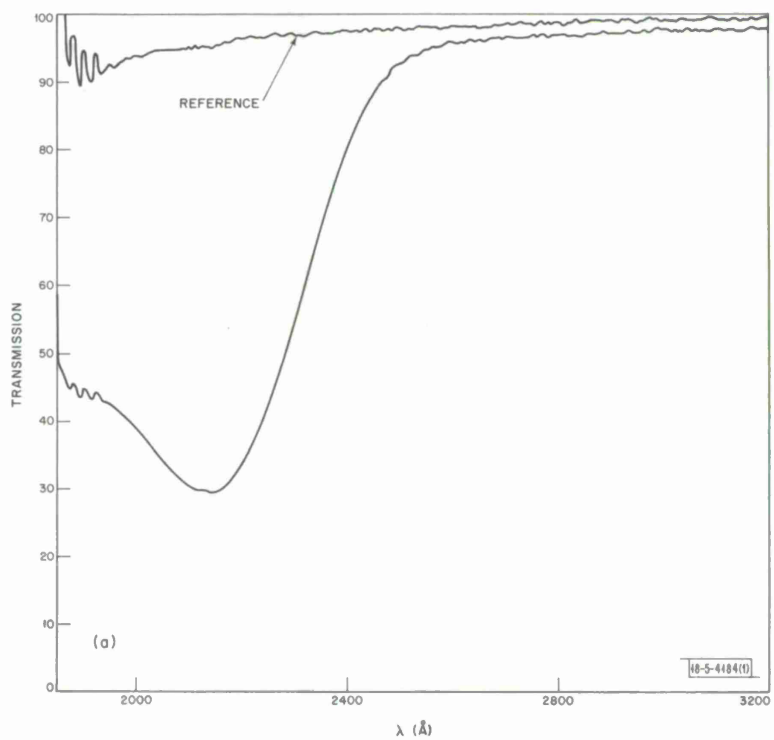


Fig. I-31. Reference absorption spectra compared with absorption spectra of (a) tripropylamine for 0.5-cm length, (b) tributylamine for 1-cm length, and (c) tripentylamine for 5-cm length.

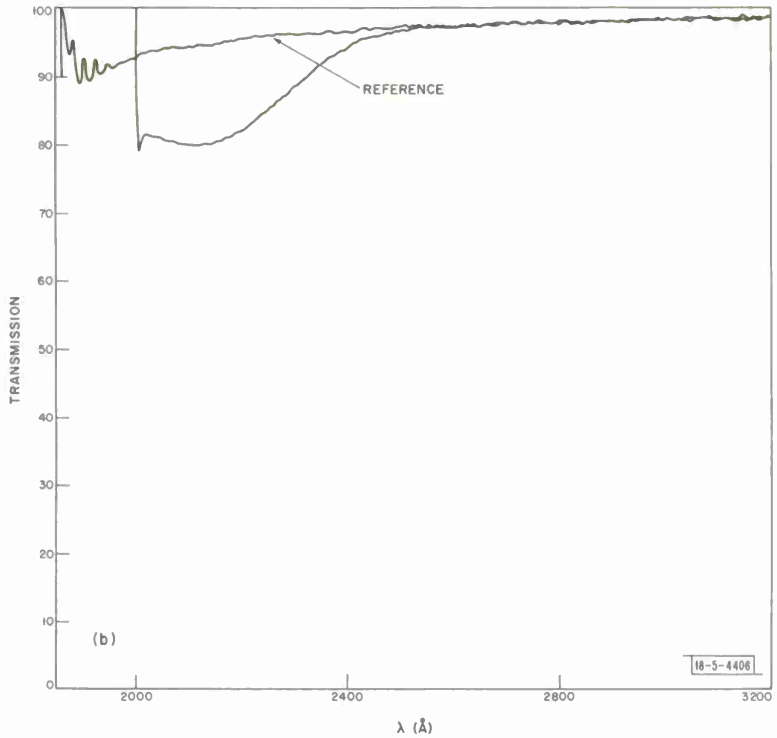


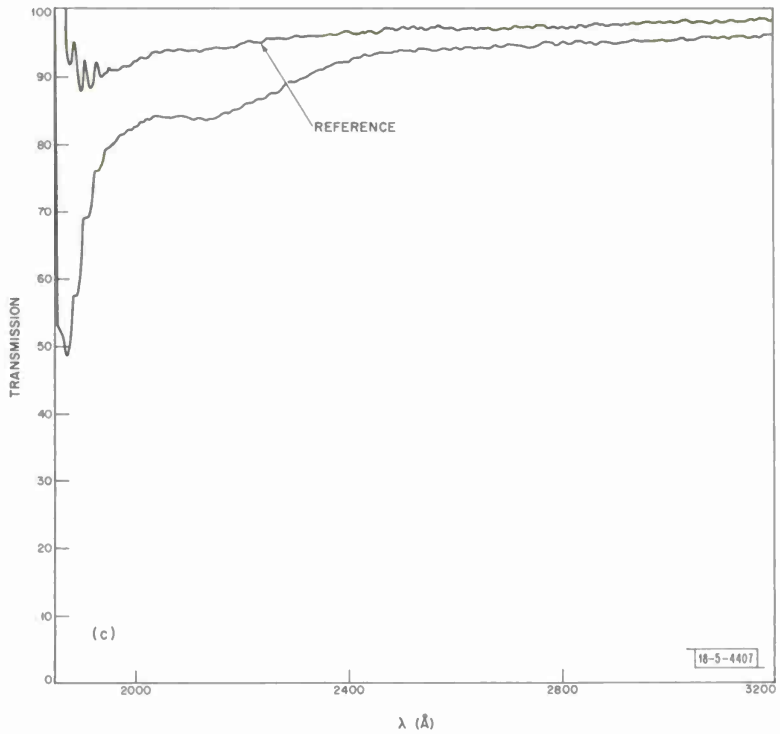


Fig. I-31. Continued.

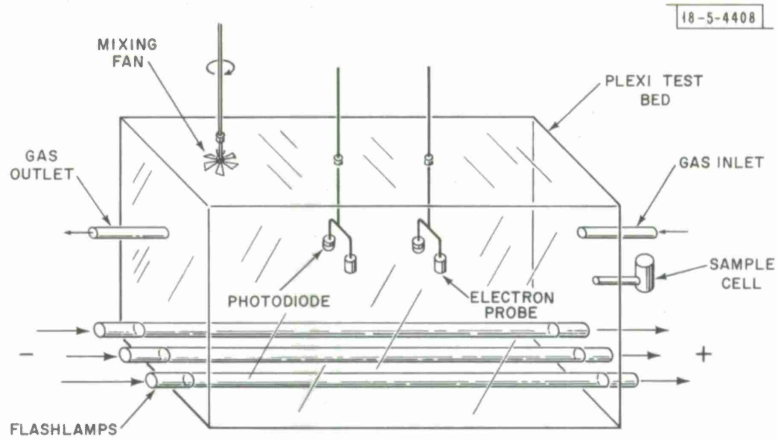


Fig. I-32. Test bed facility for measurement of photoionization distributions. Note one fixed plasma probe-photon detector set, one movable set, 3 parallel flashlamps, and sampling gas cell.

c. Test Bed

As a test bed for measurements of electron density production as a function of lamp illumination and seed concentration, we are constructing the apparatus sketched in Fig. I-32. It consists of a lucite box of internal dimensions 24 by 8 by 6 inches. At one end is a sealable cell which can be detached from the box and placed in a spectrophotometer to yield the concentration of seed molecules. Along the bottom of the box, an array of up to three flashlamps may be inserted. The top of the box contains two electron probes each with an attached photodiode, so that two simultaneous point measurements of electron density and photon flux can be made.

One probe and photodiode set is movable in a direction perpendicular to the plane of the flashlamps. In addition, provision will be made for inserting electrodes and windows so that the test bed can be converted to a laser.

d. Photon Distribution Calculations

In designing a large-volume photo-excitation laser, one of the important considerations is that of tailoring the photon distribution to yield a uniform electron density. One would also like to have a certain economy of excitation in mind so as to maximize the efficiency of the laser. We shall describe our first look at this problem, and indicate the direction of our future work.

Thus far, we have looked at three different theoretical illumination schemes:

(1) An array of linear flashlamps,

(2) Two opposing symmetric arrays of linear flashlamps,

(3) Arrays of cylindrical-elliptical cavities and cylindrical lenses.

Scheme (1) is under active consideration, since an experiment may be tried in which the present 500-J E-beam-excited laser is converted to a flashlamp-excited laser. The geometry of the machine would then dictate the first approach. Scheme (2) details the improvement in uniformity which can be achieved if opposing arrays are used. Finally, the cavity approach [scheme (3)] is used to show the improvements in efficiency that are possible.

Let us set up a coordinate system as shown in Fig. I-33 where N flashlamps of length L are located parallel to the y-axis in the x-y plane. Each lamp has a diameter of emitting volume

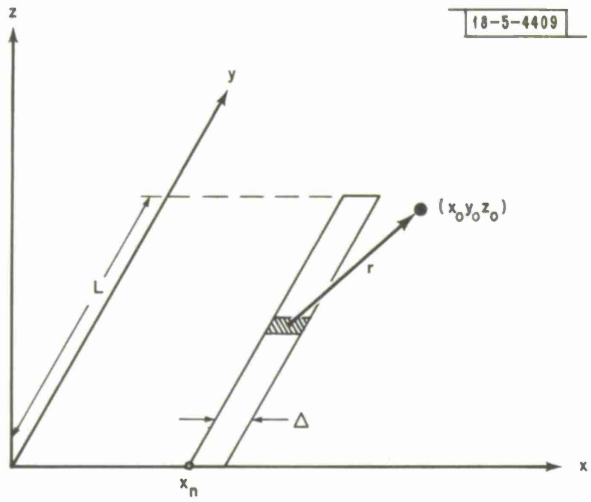


Fig. I-33. Geometry for calculating intensity distribution of flashlamp array.

equal to Δ, and the lamps start along the x-axis at points $x_n$. The brightness of each lamp is given by

$$B_n(x, y) = \begin{cases} B_n \dfrac{W}{cm^2\text{-ster}} & x_n \leqslant x \leqslant x_n + \Delta \\ & o \leqslant y \leqslant L \\ 0 & \text{elsewhere} \end{cases} .$$

Let $r^2 = z_o^2 + (x - x_o)^2 + (y - y_o)^2$.

The contribution from a single flashlamp to the intensity at point $(x_o y_o z_o)$ is

$$I_n(x_o y_o z_o) = \int_{x_n}^{x_n+\Delta} dx \int_o^L dy\, B_n \frac{z_o}{r^3} e^{-\alpha r} .$$

The total intensity at point $x_o y_o z_o$ is then

$$I(x_o y_o z_o) = \sum_{n=1}^{N} I_n .$$

Let $e^{-\alpha r} \cong 1 - \alpha r + (\alpha^2 r^2/2)$. Then, performing the y integration, we obtain

$$I_n(x_o y_o z_o) = B_n z_o \int_{x_n}^{x_n+\Delta} dx \left\{ \frac{L - y_o}{D\sqrt{(L - y_o)^2 + D}} + \frac{y_o}{D\sqrt{y_o^2 + D}} - \frac{\alpha}{\sqrt{D}} \tan^{-1} \frac{(L - y_o)}{\sqrt{D}} \right.$$

$$\left. + \frac{\alpha}{\sqrt{D}} \tan^{-1} \frac{-y_o}{\sqrt{D}} + \frac{\alpha^2}{2} \log \left( \frac{(L - y_o) + \sqrt{(L - y_o)^2 + D}}{-y_o + \sqrt{y_o^2 + D}} \right) \right\}$$

where $D = (x - x_o)^2 + z_o^2$.

Next use the approximation $r >> \Delta$ so that

$$\int_{x_n}^{x_n+\Delta} f(r)\, dx \approx f(r)\, \Delta .$$

This essentially restricts our solution to values of $z_o >> \Delta$. The solution then is

$$I_n(x_o y_o z_o) = \frac{B_n z_o \Delta}{2} \left[ \frac{L - y_o}{D\sqrt{(L - y_o)^2 + D}} + \frac{y_o}{D\sqrt{y_o^2 + D}} - \frac{\alpha}{\sqrt{D}} \tan^{-1} \frac{(L - y_o)}{\sqrt{D}} \right.$$

$$\left. + \frac{\alpha}{\sqrt{D}} \tan^{-1} \frac{-y_o}{\sqrt{D}} + \frac{\alpha^2}{2} \log\left( \frac{(L - y_o) + \sqrt{(L - y_o)^2 + D}}{-y_o + \sqrt{y_o^2 + D}} \right) \right]$$

where $D = (x_n + \Delta/2 - x_o)^2 + z_o^2$. Note that if, instead of a single array of flashlamps located at points $x_1 \ldots x_n$, we have opposing arrays of flashlamps separated by a distance H (see Fig. I-34), then $I_n(x_o y_o z_o) \rightarrow I_n(x_o y_o z_o) + I_n(x_o, y_o, H - z_o)$. This completes our solution of flashlamp arrays.

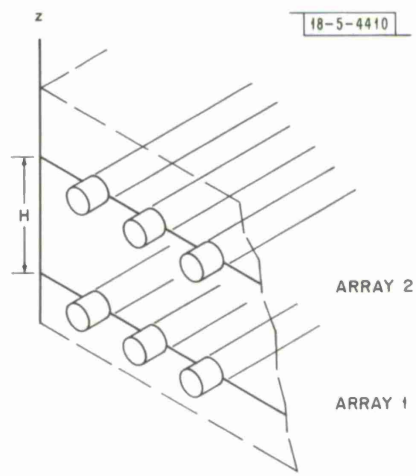


Fig. I-34. Geometry for calculating intensity distribution of opposing flashlamp arrays.

Let us now see the implication of these results using the case of 11 flashlamps, each flashlamp 112 cm long and 7 mm in diameter, with the separation between flashlamp centers equal to 15 mm. This size of array might be used to illuminate the cavity of the Lincoln Laboratory 500-J E-beam laser. Figures I-35(a) through (c) show, respectively, I(7.95, y, 10), I(x, 56, 10), and I(7.95, 56, z) for the case where $\alpha = 0$ (we neglect the effect of absorption on the photon distribution). Notice that along the x- and y-axes, one has reasonable uniformity (less than 10 percent variation over better than half the area of the cavity). In the z-direction, however, the intensity varies by a factor-of-3 going across the cavity. Figure I-36 shows the improvement attained by having opposing identical flashlamp banks separated by 20 cm. The variation in the z-direction is reduced to about 20 percent. The effect of lamp nonuniformity is shown in Figs. I-37(a) through (c) where, for the case of opposing flashlamp banks, one set of lamps (third from the end) was allowed to have 50-percent more brightness than the other lamps. On the plots, the intensities are compared with the case where all the lamps have equal intensity. The intensity effects wash out as $z >> \Delta$.

Finally we look at the effects of absorption for two cases: $\alpha = 0.01\ \text{cm}^{-1}$, and $\alpha = 0.66\ \text{cm}^{-1}$. The intensity I(7.95, 56, z) for opposing flashlamp banks is shown for these two cases as well as $\alpha = 0$ in Fig. I-38. As might be expected, absorption increases the nonuniformity by reducing the intensity at the center of the cavity.

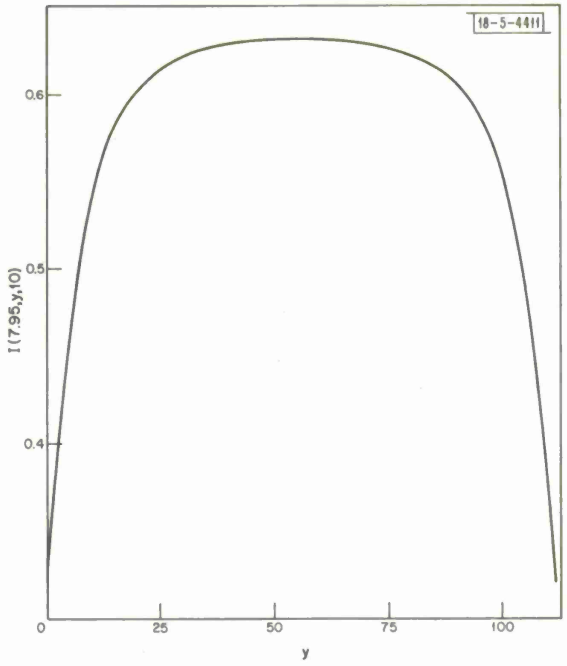


(a) Distribution parallel to y-axis.

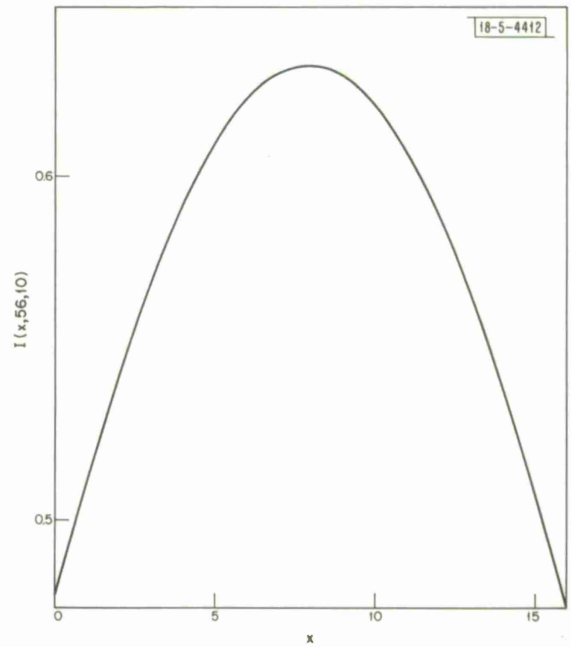


(b) Distribution parallel to x-axis.

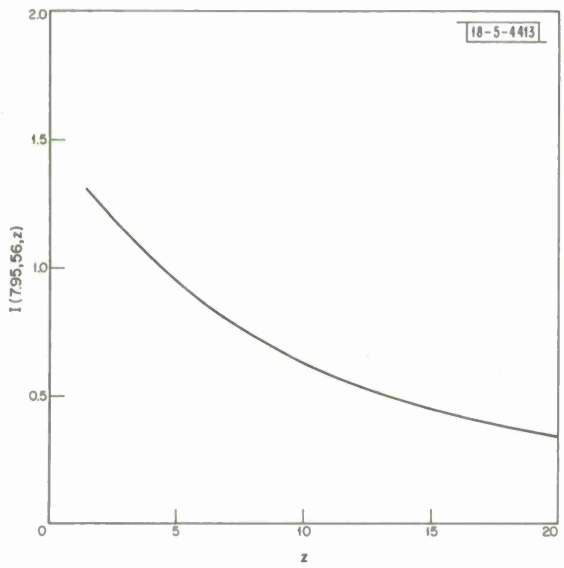


(c) Distribution parallel to z-axis.

Fig. I-35(a-c). Calculated intensity distribution for single-flashlamp array.

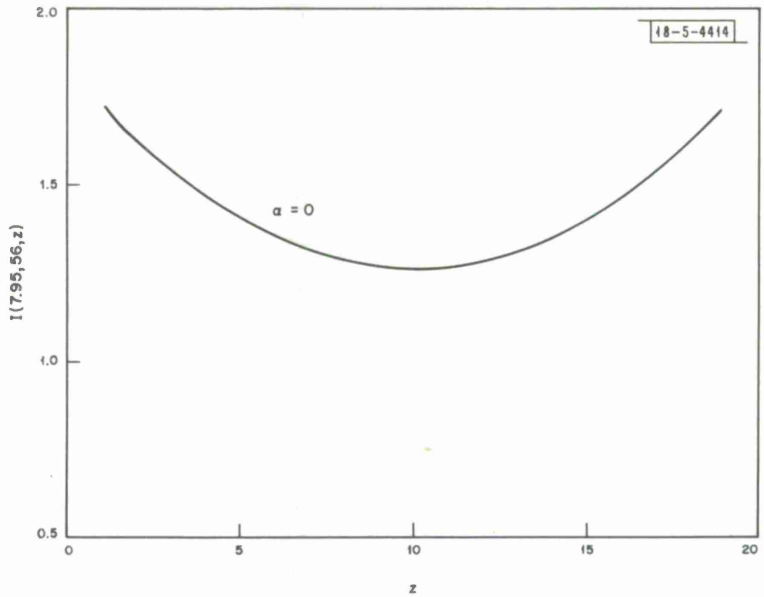


Fig. I-36. Intensity distribution parallel to z-axis for opposing flashlamp arrays.

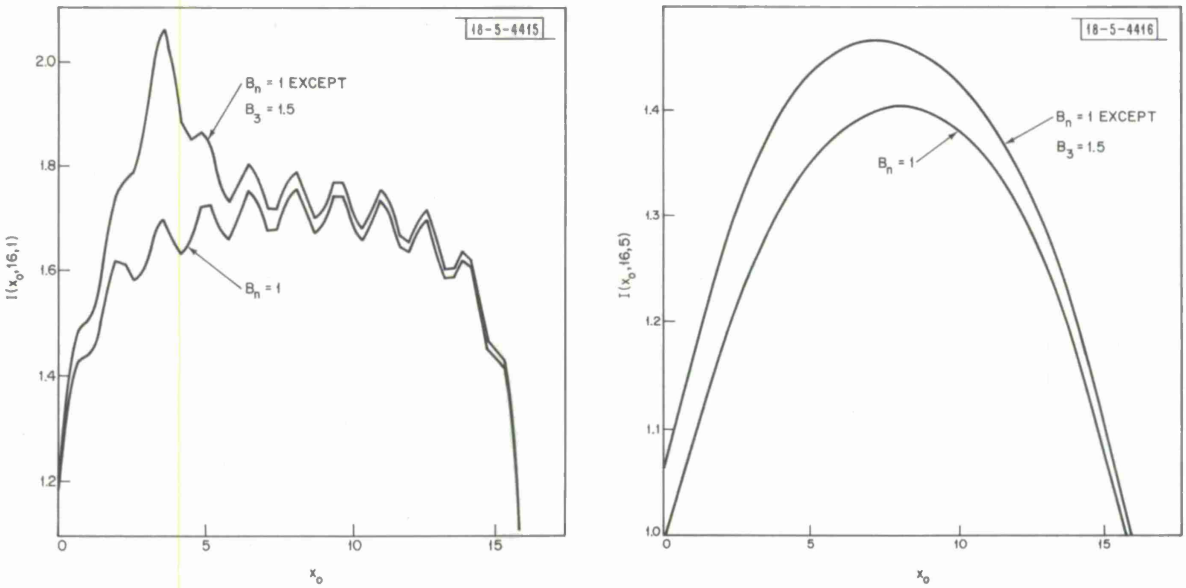


(a) I(x, 16, 1).

(b) I(x, 16, 5).

Fig. I-37(a-c). Variation in intensity distribution if one flashlamp in array is 50-percent brighter than remaining flashlamps. Displayed here are distributions parallel to x-axis for opposing flashlamp arrays with tube 3 50-percent brighter in both arrays for different positions $z_o$.

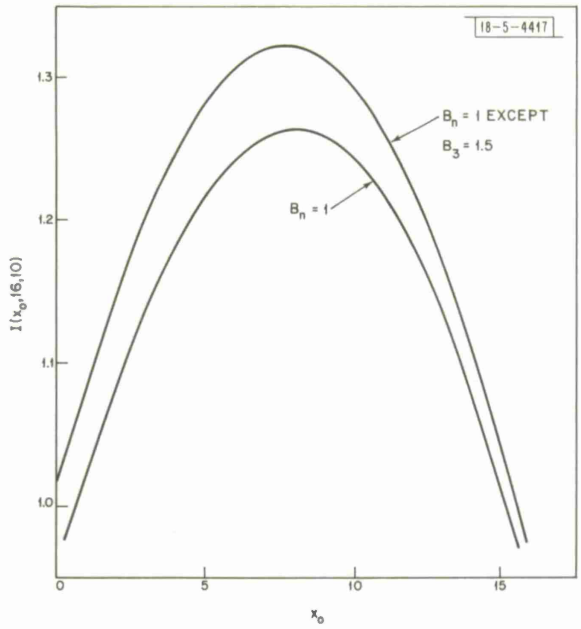


(c) I(x, 16, 10).

Fig. I-37(a-c). Continued.

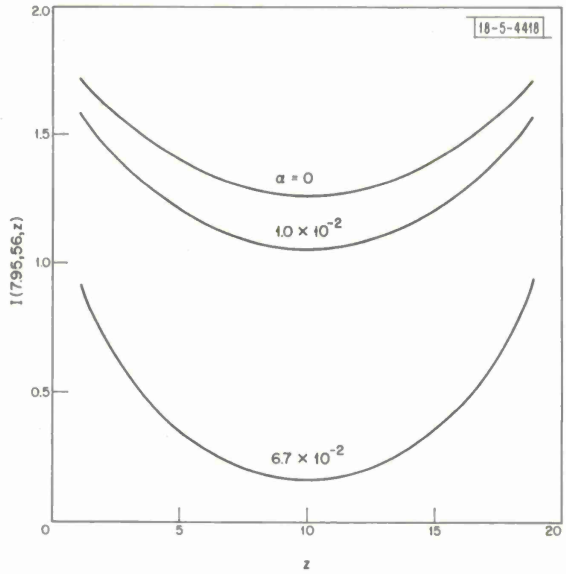


Fig. I-38. Intensity distribution for opposing flashlamp arrays as function of absorption coefficient $\alpha$.

One can increase the uniformity as well as the effective brightness of a flashlamp by using an enclosing cavity and collimating optics. One cavity to consider is a one-dimensional variant of the ellipsoidal-spherical cavity described by N. G. Mikhailus'.[21] Figure I-39 gives an end view of such a cavity. For perfectly reflecting cavity walls, the effective brightness of the imaged source is $4B_0$ (as the radiation is sent in a 90° cone rather than 360°) and, effectively, 100 percent of the photons may be captured by a lens of the proper design, collimated and used to illuminate a laser cavity.

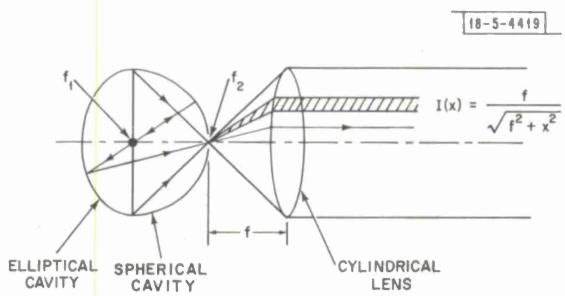


Fig. I-39. Cross-sectional sketch of possible cavity illumination technique. Here, $f_1$ and $f_2$ are focal points of elliptical cross section; and $f_1$ is, additionally, center of circular cross section. I(x) is intensity present when single cavity is used to illuminate laser medium.

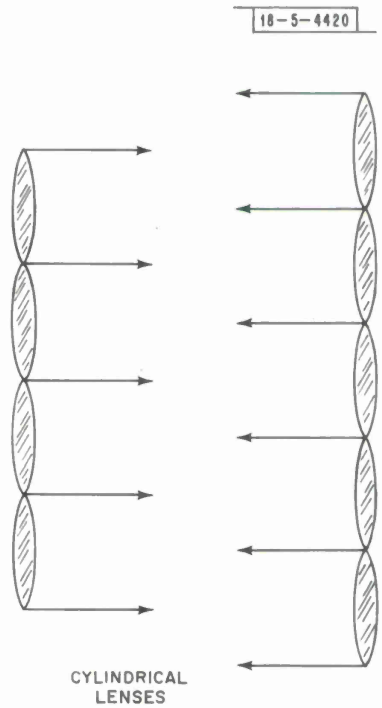


Fig. I-40. Possible optical arrangement to minimize intensity variations when using elliptical-circular cavities.

Neglecting absorption again, a design such as this gives no variation along the z-axis (direction of light propagation) or y-axis (axis of the sphero-elliptical cavity), but there will be a variation along the x-axis:

$$I(x) = \frac{f}{\sqrt{f^2 + x^2}} \quad .$$

(See Fig. I-39, because the light source emits cylindrical waves and the collimating optics is planar.) If one uses fast optics (f/1) to collect all the emitted light, this will lead to a 30-percent variation across the diameter of the lens. However, by using an arrangement of opposing displaced lenses (Fig. I-40), the intensity variation becomes

$$I(x) = \frac{1}{\sqrt{1 + (x/f)^2}} + \frac{1}{\sqrt{1 + \left(\frac{H - x}{f}\right)^2}}$$

and for f/1 optics this reduces the x-variation to less than 5 percent. The practicality of configuring such a cavity with sufficiently high UV reflectivity and coupling it to a quartz cylindrical lens has not yet been ascertained.

H. Granek S. Marcus
H. Kleiman R. W. O'Neil

7. Laser Power Amplifier Study

Investigations have been made of the feasibility of amplifying pulses of 100-μsec duration and longer at a prf of 100 Hz with a total output of 200 J per pulse and good beam quality and stability. Preliminary studies were reported earlier (see Ref. 1, p. 43). Here, we summarize the conceptual designs of an unsaturated and a saturated amplifier based on computations with a five-temperature model (see Ref. 1, p. 37) of the $CO_2$-$N_2$ gas kinetics. The five temperatures describe the energy distribution in each of the three $CO_2$ vibrational modes, in the nitrogen vibrational mode, and in the gas translational motion. A more complete description of the results is given elsewhere.[22]

In an unsaturated mode with flux densities not exceeding one-tenth of the saturation intensity, the laser described by Table I-1 and shown in Fig. I-41 would provide 33-dB total gain with an output of 200 J in 100 μsec. However, the system was felt to be excessively large and inefficient; therefore, a fully saturated amplifier was considered. The parameters of this system are shown in Table I-2.

Finally, we have preliminary results on a model of the saturated amplifier system with fast gas flow and find indeed that a CW mode of operation for the E-beam-excited laser would allow very long pulse amplification with a small-signal gain of as much as 0.9 percent/cm. The small signal gain history of this CW amplifier is shown in Fig. I-42. Compared with the pulse amplifier, the CW amplifier has a reduced E-beam current, enhanced flow, and reduced initial temperature.

H. Granek
D. M. Zanni*
T. J. Gilmartin

8. $C^{13}O_2^{16}$ Isotope Lasers

We have obtained very satisfactory operation with a $C^{13}O_2^{16}$ isotope in our grating-controlled stable lasers. The power outputs and the gains of the various lasing transitions appear to be comparable or just slightly less than in $C^{12}O_2^{16}$ lasers.

In the preliminary measurements, we used a SPEX 1703 spectrometer to determine the wavelengths of 72 lasing transitions in the P- and Q-branches of the 001 to 100 and the 001 to 020 vibrational bands. The estimated accuracy of the spectrometer data is better than 0.04 wavenumber. These spectrometer data were then utilized to select pairs of transitions from the $C^{12}O_2^{16}$ and $C^{13}O_2^{16}$ spectra which were closest in frequency. We then utilized two grating-controlled stable lasers filled with $C^{12}O_2^{16}$ and $C^{13}O_2^{16}$ isotopes, respectively, to heterodyne a number of the adjacent lasing transitions. The frequencies we have so far measured ranged from 325-MHz beat note of the $C^{12}O_2^{16}$ (001 to 020) vibrational band P(28) and the $C^{13}O_2^{16}$ (001 to 020) vibrational band R(28) lines to the 18-GHz beat note of the $C^{12}O_2^{16}$ (001 to 100) band P(24) and the $C^{13}O_2^{16}$ (001 to 100) band R(38) transitions.

---

* Philco Corporation.

TABLE I-1

SPECIFICATIONS FOR LASER POWER AMPLIFIER IN UNSATURATED MODE

| | |
|---|---|
| Type | E-beam excited |
| Pressure | 250 torrs |
| Mixture | Nominal $He:N_2:CO_2$; 3:2:1 |
| Flow rate | $7 \times 10^3$ to $10^4$ cm/sec |
| Cross section at last stage | 3200 $cm^2$ |
| Total gain | 33 dB |
| Nominal small-signal maximum gain | 0.01155 $cm^{-1}$ |
| Discharge length | 64 cm |
| Transverse width | 64 cm |
| Sustainer voltage | Nominal 100 kV |
| Length | 7 m |
| Primary beam | $\sim 7.3 \times 10^{-6}$ $A/cm^2$ |
| Accelerating voltage | $\leqslant$250 kV |

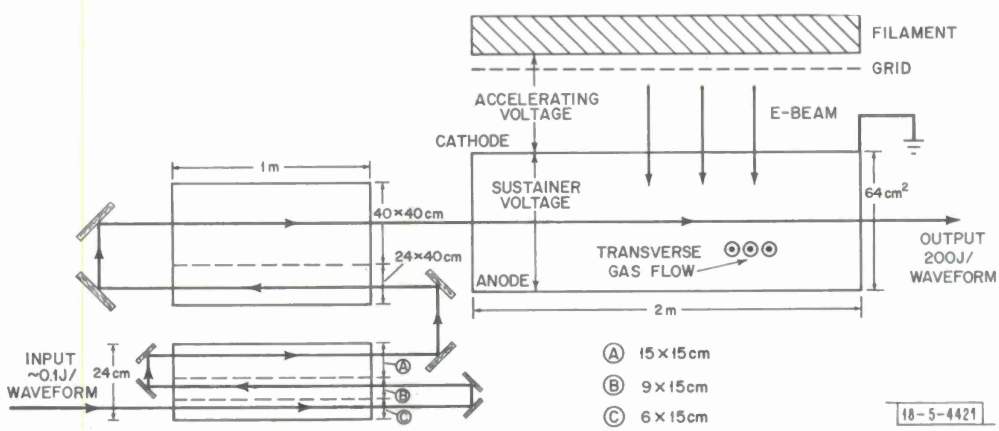


Fig. I-41. Schematic of E-beam ionized laser operating in unsaturated mode. Seven meters of gain length are folded into 3 devices: 1 M × 24 cm × 15 cm; 1 M × 64 cm × 40 cm; and 2 M × 64 cm × 64 cm. A net power gain of 33 dB, producing 200-J output in 100 μsec, is obtainable.

TABLE I-2

PARAMETERS OF LASER POWER AMPLIFIER IN SATURATED MODE

| | |
|---|---|
| Dimensions of chamber | 100 cm long<br>15 cm high<br>15 cm wide |
| Volume of chamber | 22.5 liters |
| Volume utilized | 14 liters |
| Pressure | 250 torrs |
| Gas mixture | 3:3:1; $He:N_2:CO_2$ |
| Number of passes | 12 (6 at 0.5-cm initial diameter, and 6 at 5-cm diameter) |
| E-beam current density | $10^{-4}$ A/cm$^2$ |
| E-beam voltage | 200 kV before foil<br>160 kV after foil |
| E-beam area | 1500 cm$^2$ |
| E-beam current | 150 mH |
| E-beam peak power | 30 kW |
| E-beam average power | 600 W |
| Sustainer-current density | 0.5 A/cm$^2$ |
| Sustainer current | 750 A |
| Sustainer voltage | 25.5 kV |
| Sustainer peak power | 20 MW |
| Sustainer average power | 400 kW |
| Total peak gain | 32 dB |
| Small-signal gain | 2.2 percent cm$^{-1}$ = 9.5 dB/m |
| Saturated gain | 220 W/cm$^3$ |
| Saturation flux | 10 kW/cm$^2$ |
| Peak output power | 1.5 MW |
| Average output power | 20 kW |
| Overall efficiency | 5 percent |
| Gas-flow velocity | 15 m/sec |
| Gas-flow rate | 750 liters/sec STP |

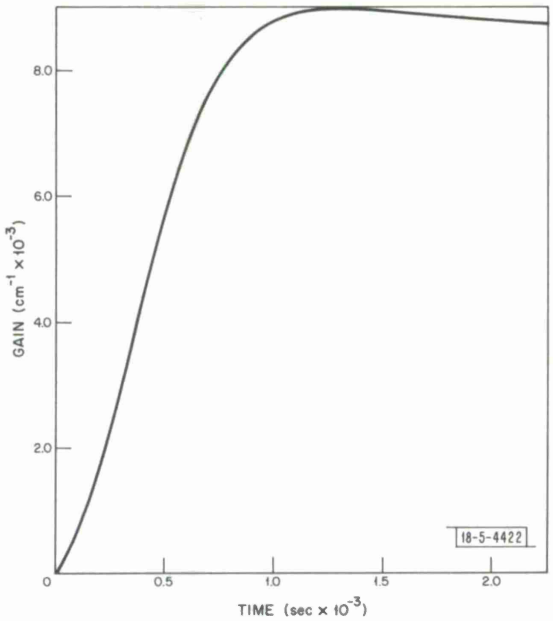


Fig. I-42. Approach to CW operation in E-beam laser. Initial gas temperature 210°C, 3:2:1 mixture of $He:N_2:CO_2$ at 250 torrs, $J_{prim} = 10^{-6}$ A/cm$^2$, E = 1.7 kV/cm, and mean time of particle in active region = $5 \times 10^{-4}$ sec.

In the heterodyne experiments, we used very fast, back-biased HgCdTe detectors made by D. L. Spears in Lincoln Laboratory. Continuation of these experiments should accurately determine the beat-note frequencies up to at least 35 GHz.

C. Freed

## REFERENCES


1. Optics Research Report, Lincoln Laboratory, M.I.T. (1972:1), p. 1, DDC AD-754939.
2. See, for example, W. G. Davenport, Jr. and W. L. Root, Random Signals and Noise (McGraw-Hill, New York, 1958), Sec. 6-4.
3. R. Schlier, Avco-Everett Research Laboratory, personal communication.
4. S. Marcus, Appl. Phys. Letters 21, 18 (1972), DDC AD-752953.
5. D. B. Chang, J. E. Drummond and R. B. Hall, J. Appl. Phys. 41, 4851 (1970).
6. Ya. B. Zel'dovich and Yu. P. Raizer, Physics of Shock Waves and High-Temperature Hydrodynamic Phenomena. VI (Academic Press, New York, 1966), p. 97.
7. R. Schlier, private communication.
8. J. F. Ready, Effects of High-Power Laser Radiation (Academic Press, New York, 1971), p. 100.
9. H. B. Palmer and M. Shelef, "Vaporization of Carbon," in Chemistry and Physics of Carbon, Vol. 4, P. L. Walter, Jr., Ed. (Marcel Dekker, Inc., New York, 1968).
10. D. W. Gregg and S. J. Thomas, J. Appl. Phys. 37, 2838 (1966).
11. D. Smith and P. J. Berger, private communication.
12. R. Schlier, private communication.
13. L. C. Marquet, Appl. Opt. 10, 960 (1971), DDC AD-729610.
14. R. W. O'Neil, et al., "High-Energy Pulsed $CO_2$ Laser-Target Interaction in Air," LTP-17, Lincoln Laboratory, M.I.T. (28 September 1972), DDC AD-896666-L.
15. A. F. Gibson, M. F. Kimmitt and A. C. Walker, Appl. Phys. Letters 17, 75 (1970).
16. H. Kleiman and S. Marcus, "$CO_2$ Laser Pulse Shaping with Saturable Absorbers," J. Appl. Phys. (to be published).
17. A. Javan and J. S. Levine, IEEE J. Quantum Electron. QE-8, 827 (1972), DDC AD-753308.
18. S. C. Brown, Basic Data of Plasma Physics (M.I.T. Press, Cambridge, 1959).
19. C. A. Fenstermacher, M. J. Mutter, W. T. Leland and K. Boyer, Appl. Phys. Letters 20, 56 (1972).
20. J. S. Levine and A. Javan, Appl. Phys. Letters 22, 55 (1973).
21. N. G. Mikhailus', J. Appl. Spectrosc. 11, 1123 (1969) (Russian translation).
22. H. Granek, LTP-21 (in preparation).

# II. OPTICAL MEASUREMENTS AND INSTRUMENTATION

## A. A VERY RAPID INTERFEROMETRIC TECHNIQUE FOR VISIBLE AND IR MTF MEASUREMENTS

Previous modulation transfer function (MTF) measurements, using a corner-cube shearing interferometer, have been carried out from a KC-135 jet aircraft flying at normal altitude and speed.[1] The nature of imaging through the atmosphere is such that the MTF is changing from one instant to the next, and from an airborne platform the changes may occur as rapidly as 1 msec. Hence, it is desirable to have an MTF measuring system that can obtain the complete MTF curve (for all shear values or spatial frequencies) in as short a time as possible, and close to 1 msec. Therefore, for future airborne experiments, a new, continuously shearing and scanning-type interferometer has been designed and laboratory-tested. A simple triangular interferometric configuration has been employed, similar in concept to that described by Hariharan and Sen.[2] However, unlike their system, which employed a polarization technique, a much simpler path-changing operation has been employed. Both the shearing and path-changing effects in the new interferometer are produced simply by continuous rotation of the micrometer plate, and are described below. In this way, the discontinuities and nonlinearities associated with the piezoelectrically scanned interferometer are avoided. A smooth, continuous, constant-frequency carrier signal is generated as the shear is continuously varied, which allows better narrow-band electronic filtering and, consequently, better signal-to-noise ratios at the high shear values.

An optical schematic of the triangular interferometer is shown in Fig. II-1. An incident collimated beam of light is divided into two parts at the beam splitter, and then each beam traverses the triangular-path interferometer in opposite directions to be recombined and interfere at the beam splitter again. The light is subsequently directed to a photomultiplier. The micrometer plate, when rotated through an angle $\Theta$ from a normal symmetrical position, will both change

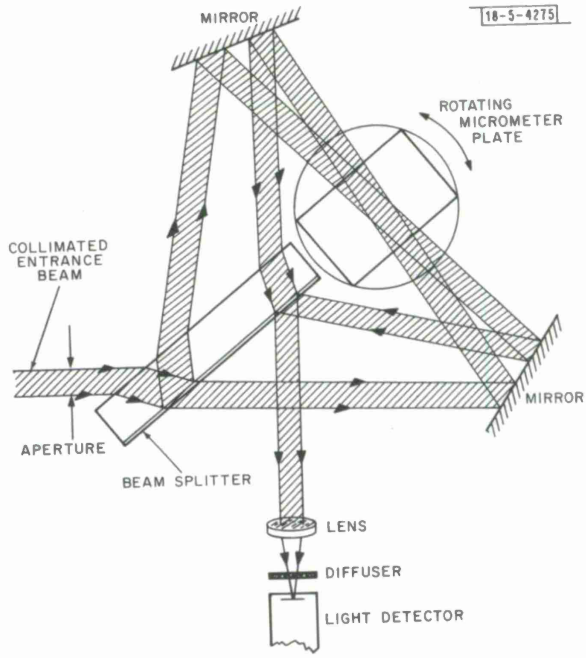


Fig. II-1. Triangular interferometer for rapid MTF measurement.

the path length each beam traverses through the interferometer and produce equal but opposite amounts of lateral displacement or shear of the two beams. For each beam, as the micrometer plate is rotated from the normal through an angle $\Theta$, the total path change is given by

$$\Delta = (\mu - 1)\, t + \frac{(\mu - 1)\, t}{2\mu}\, \Theta^2$$

where $\mu$ is the refractive index, t is the plate thickness, and $\Theta$ is the angle between the normal to the plate and the beam traversing it. If the interferometer is set up so that the two beams traversing the plate are not parallel, but each makes a slightly different angle to the normal, $\Theta_1$ and $\Theta_2$, respectively, as shown in Fig. II-1, then the path change in each case is not equal, but depends on the angle:

$$\text{Beam 1} \qquad \Delta_1 = (\mu - 1)\, t + \frac{(\mu - 1)\, t}{2\mu}\, \Theta_1^2$$

$$\text{Beam 2} \qquad \Delta_2 = (\mu - 1)\, t + \frac{(\mu - 1)\, t}{2\mu}\, \Theta_2^2 \quad .$$

Therefore, the relative difference in path length for the two beams is given by

$$\Delta = \Delta_1 - \Delta_2 = \frac{(\mu - 1)\, t}{2\mu}\, (\Theta_1^2 - \Theta_2^2)$$

or

$$\Delta = \frac{(\mu - 1)\, t}{2\mu}\, (\Theta_1 + \Theta_2)\, (\Theta_1 - \Theta_2) \quad .$$

If the micrometer plate is rotated continuously and uniformly, the path mismatch in the two beams varies linearly with the angle of rotation, since $(\Theta_1 - \Theta_2)$ is constant. The relative shear (lateral displacement) of the two beams is given by

$$s = 2\, \frac{(\mu - 1)}{\mu}\, \frac{t}{h}\, (\Theta_1 + \Theta_2)$$

where h = beam diameter. Therefore, both shear, s, and path difference vary linearly with $(\Theta_1 + \Theta_2)$. As the micrometer plate is rotated, the output signal (measuring the total light in the interferogram) consists of a constant-frequency carrier signal, whose amplitude is modulated continuously. This output signal traces directly the complete MTF curve and can be recorded on tape and displayed visually in real time on an oscilloscope.

A laboratory system was set up, the micrometer plate being continuously rotated by a small DC motor. The display on the oscilloscope for a 10-mm diffraction-limited circular aperture is shown in Fig. II-2. For each rotation of the micrometer plate, the complete MTF (from s = 0 to s = 2) is obtained four times. Part of the scanning time must necessarily be dead time. In practice, the parameters are chosen so that a complete MTF curve is traced as the micrometer plate is rotated through about 20°. Hence, for each rotation, approximately 75 percent of the time is dead time. The display shown in Fig. II-2 corresponds very closely to the diffraction-limited curve for a clear aperture, the time scale being about 50 msec for the complete MTF curve. In the laboratory, rotating the micrometer plate at 3000 rpm, the complete MTF curve has been measured in roughly 1.5 msec. The carrier signal in this case was somewhere between 10 and 100 kHz (this depends on $\Theta_1 - \Theta_2$).

This new interferometric method for measuring the MTF is much simpler than any of the previous techniques employed and is capable of very fast monitoring of the complete MTF curve.

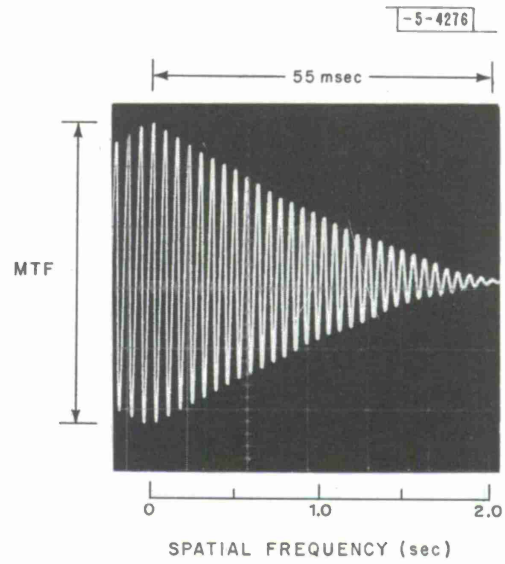


Fig. II-2. MTF (circular aperture) with triangular interferometer.

The curve can be obtained with a scan rate less than 1 msec. It therefore will be ideally suited to both airborne and ground-based atmospheric MTF measurement studies.

The new method is well suited to extension to IR measurements up to 10 μm, if the micrometer plate and the beam splitter are chosen to be of a suitable material for this wavelength region, and if an IR detector is used. In this case, because of the longer wavelengths and other parameters, the maximum useful scan rate may be somewhat less than that in the visible version of this interferometer.

Nevertheless, the data-gathering capability of this new technique exceeds any other known MTF measuring systems and is amenable to relatively simple digitization and computer-processing operations. It is, of course, necessary to employ a monochromatic coherent-radiation laser source, which in the case of atmospheric propagation studies at the present time, is perfectly convenient. The triangular interferometer will be ruggedized and capable of operating from the KC-135 airborne platform, as was the corner-cube interferometer described earlier. Because of the simpler optical components, it will be more compact than the previous system, and as before, will not require any internal adjustments during use.

D. Kelsall

## B. ATMOSPHERIC OPTICAL COHERENCE MEASUREMENTS AT 10.6 AND 0.63 μm

A brief description of the experimental setup and of the preliminary results has previously been reported.[3] For the convenience of the reader we will reiterate some details. Three measurements were made. First, at the Lincoln Laboratory Firepond Site a 5-W, 10.6-μm Gaussian beam 136 cm in diameter at $e^{-2}$ power was projected from a Cassegrainian telescope with a 122-cm aperture diameter and a 40-cm central shadow diameter and was focused on a diffuse Al plate mounted on the Groton Firetower at a range of 5.4 km. The resultant image was scanned by an IR imaging camera, video recorded and later analyzed in a digital computer. The propagation path shown in Fig. II-3 was about 68 m above irregular wooded terrain. Second, a 10-mW divergent 0.63-μm source located near the Al plate was observed from a position near the Cassegrainian telescope by means of an 8.9-cm Questar telescope. The latter telescope was equipped

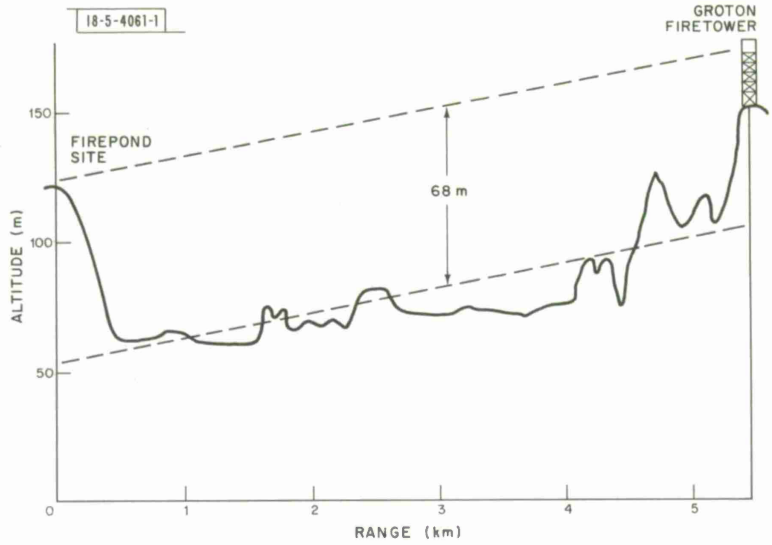


Fig. II-3. Propagation path.

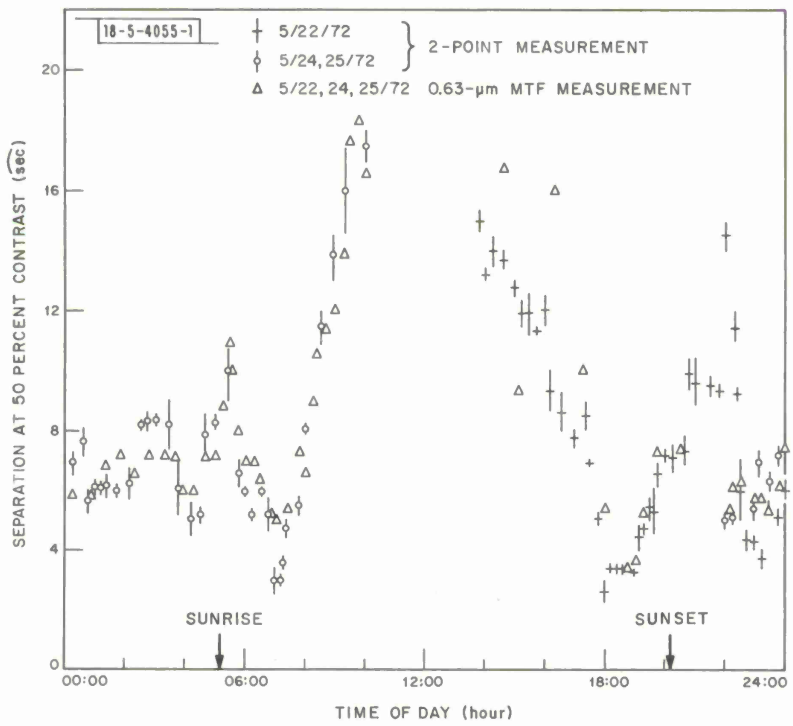


Fig. II-4. Measured diurnal variation of atmospheric seeing.

with an instrument which measured directly the MTF at 0.63 μm (Ref. 4). Third, a human observer located near the Cassegrainian telescope used a second 8.9-cm Questar telescope to observe two white-light point sources of variable separation[5] located near the Al plate. While being careful to maintain a constant apparent brightness of the sources by means of neutral density filters placed in the eyepiece of the second Questar telescope, this observer determined the separation at which the two sources were resolved with 50-percent contrast. These three measurements were made approximately simultaneously about every 15 minutes for portions of several days until data for a complete diurnal cycle had been obtained.

1. Visible Measurements

Figure II-4 shows the resolution allowed by the atmosphere over our propagation path in terms of the angular separation of bar pairs (MTF instrument) or point sources (human observer) which can be resolved with 50-percent contrast. The data cover the diurnal cycle under clear skies and illustrate the cycle's commonly observed features: namely, very poor seeing during the day, better seeing at night, excellent seeing after sunrise and before sunset (as the temperature lapse is reversing), and short periods of good seeing before sunrise and poor seeing after sunset. The data obtained by these two techniques are very well correlated. While the MTF measurements yield a more complete representation of the atmospheric contrast function, the two point-source observation is much more easily implemented. In either case, as will be illustrated below, we are now confident that these techniques can be used to obtain measurements of atmospheric seeing which will allow prediction of the effects of the atmosphere on a 10.6-μm beam.

2. 10.6-μm Measurements

The diurnal variation of the short- and long-exposure spot sizes and of the spot wander at 10.6 μm are shown in Fig. II-5. Qualitatively, these spot characteristics follow the same cycle

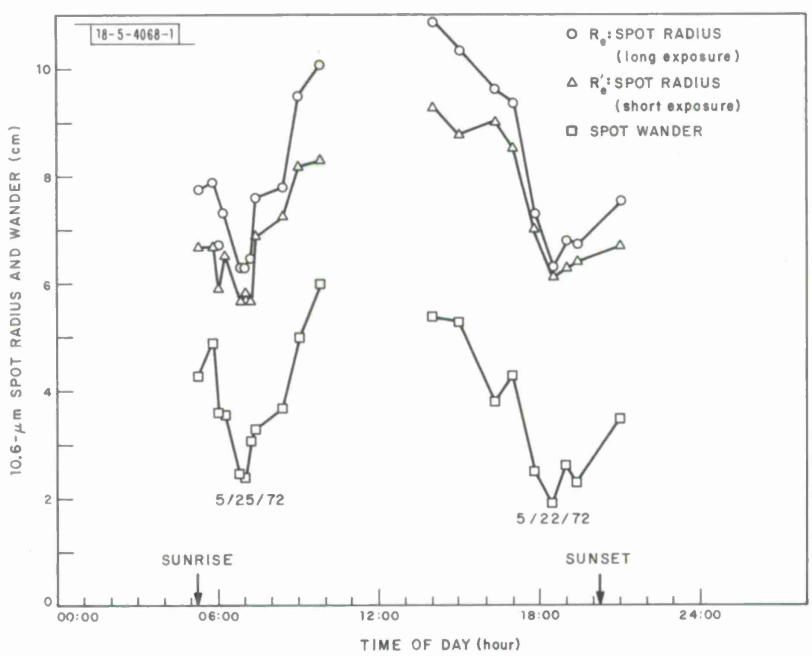


Fig. II-5. Diurnal variation of 10.6-μm spot characteristics.

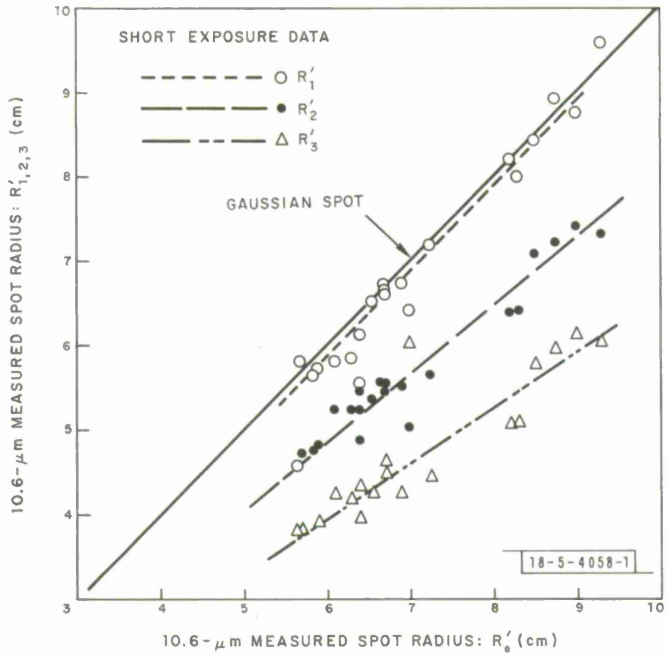


Fig. II-6. Comparison of various measures of spot size (short exposure data).

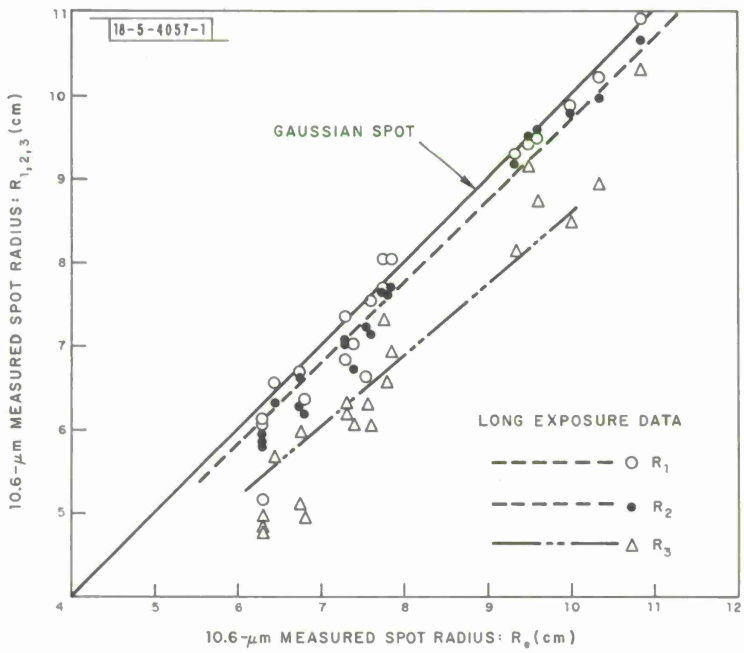


Fig. II-7. Comparison of various measures of spot size (long exposure data).

as does the visible seeing (resolution) in Fig. II-4. For these curves, the 10.6-μm spot radii $R_e$ and $R'_e$ (prime indicates short exposure) are the radii measured from the spot center, within which is contained all but the $e^{-1}$ of the power incident on the Al plate. $R'_e$ is the average of the radii computed for each of 50 single-frame images of the spot obtained with the IR camera at $\frac{1}{2}$-sec intervals over 25 sec. The exposure time is 50 msec. $R_e$ is the radius computed for a single composite frame formed by superimposing the 50 frames used to obtain $R'_e$. The exposure time for $R_e$ is 25 sec. The spot wander is the rms deviation of the spot from its average position computed from the same 50 frames.

While $R_e$ is a simple and convenient experimental measure of the flux concentration, which is readily obtained by means of computer analysis of actual flux distributions, it is difficult to work with analytically and is not used by theorists. Three measures of the spot size which are often used are defined in Table II-1 in terms of the flux or intensity distribution $I(r, \Theta)$. These measures are normalized so that if $I(r, \Theta)$ is a Gaussian distribution, then $R_e = R_1 = R_2 = R_3$. An experimental comparison of these three measures with $R_e$ is shown in Figs. II-6 and II-7. The $R_1$ is infinite for an Airy pattern and would appear to be a poor indicator, because it so heavily weights the flux away from the spot center. However, our results show it to be the bes. indicator of $R_e$ and most consistent for short and long exposures and from good to poor seeing.

TABLE II-1

DEFINITIONS OF SPOT SIZE: $R_1$, $R_2$, $R_3$

$$R_1 = R_{rms} \quad ,$$

$$R_2 = (I_1^2/2\pi I_2)^{1/2} \quad ,$$

$$R_3 = (I_1/\pi I_o)^{1/2} \quad ,$$

and $R_e$, defined as an integration limit, is

$$e^{-1} = \int_o^{2\pi} \int_{R_e}^{\infty} I(r, \Theta)\ r dr d\Theta \quad ,$$

where

$$I_o = \text{peak of } I(r, \Theta) \quad ,$$

$$I_1 = \int_o^{2\pi} \int_o^{\infty} I(r, \Theta)\ r dr d\Theta \quad ,$$

$$I_2 = \int_o^{2\pi} \int_o^{\infty} I^2(r, \Theta)\ r dr d\Theta \quad ,$$

and

$$R_{rms}^2 = \int_o^{2\pi} \int_o^{\infty} [I(r, \Theta)/I_1]\ r^3 dr d\Theta$$

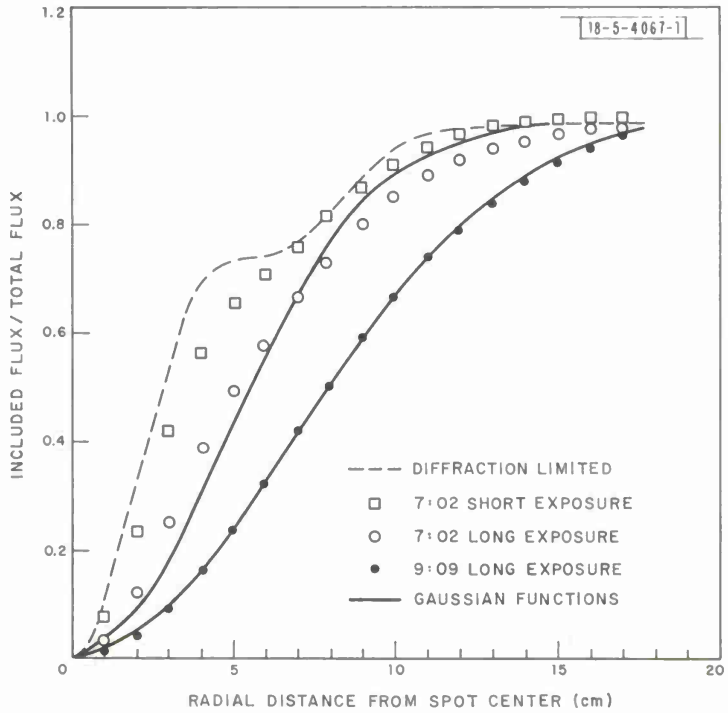


Fig. II-8. Typical flux distributions for good (7:02) and bad (9:09) seeing conditions.

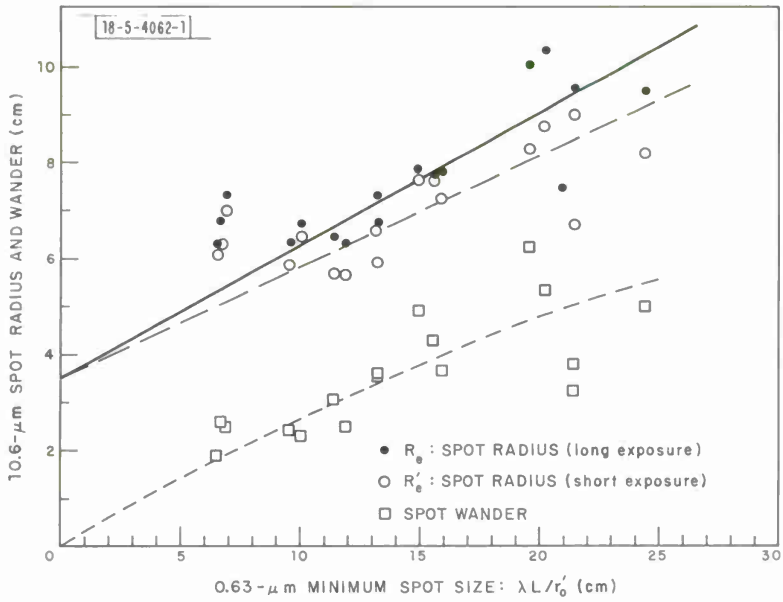


Fig. II-9. Correlation of 10.6-μm spot characteristics and 0.63-μm coherence diameter.

Our data may bias this judgment by eliminating the most strongly weighted area because our computation is truncated at ±25 cm in both x and y by the field of view of the IR imaging camera. This field should be compared with the typical spot diameter of 10 to 15 cm. The $R_2$, which is well behaved analytically even in the presence of intensity noise, is also a good experimental indicator of $R_e$. When used on the short exposure data for which the intensity distribution tends to be more peaked and less Gaussian, the $R_2$ slightly underestimates $R_e$. For the long exposure data, $R_2$ is an excellent indicator of $R_e$. The $R_3$, on the other hand, underestimates $R_e$ for both short and long exposure data, the discrepancy being greater for the short exposure data. On the basis of comparison with $R_e$, $R_1$ and $R_2$ are the better measures of the spot size.

The variation in spot shape or flux distribution, as the seeing deteriorates, is shown in Fig. II-8. The best single short exposure (7:02) is only slightly degraded from the computed diffraction-limited distribution. The long exposure distribution (7:02), even with good seeing, is noticeably deteriorated, but not Gaussian. By 9:09 the seeing had become poor and the long exposure distribution is very well fit by a Gaussian function. The implication of this is that the atmospheric MTF becomes Gaussian under poor seeing conditions, that is, becomes exponentially dependent upon the 6/3 power of spatial frequency, rather than the predicted 5/3 power.[6]

3. Comparison of Visible and 10.6-μm Measurements

A comparison of visible and IR data is given in Fig. II-9, which shows the correlation between the spot radii (both short and long exposures) and the spot wander of the focused 10.6-μm beam, and the atmospheric coherence diameter measured at 0.63 μm with the MTF instrument. The curves shown are fits to the data.

The 0.63-μm short exposure coherence diameter $r_o'$ is used in the form of the minimum achievable spot size $\lambda L/r_o'$, where $\lambda = 0.63$ μm and $L = 5.4$ km, because this parameter is a measure of the atmospherically allowed resolution at 0.63 μm, and thus affords a direct comparison with the spot size and spot wander observed at 10.6 μm. The fact that $\lambda L/r_o'$ is larger than the observed 10.6-μm spot size is indicative of the fact that the atmospherically limited resolution improves with wavelength. The short exposure 0.63-μm coherence diameter was obtained from the MTF measurements by computing $\Re = \int \mathrm{MTF}(f)\, f df$ for the data and comparing this "resolution" with the same quantity computed from theory by using Fried's analysis.[6] The theoretical $\Re$ normalized by the instrument resolution $\Re_I$ is shown in Fig. II-10 as a function of the ratio of the telescope diameter to the coherence diameter $D/r_o$. This theoretical computation utilized the actual aperture shape of the Questar telescope. The designations LE, SEFF and SENF refer to the long exposure, short exposure far field and short exposure near field cases, respectively. Figure II-10 can also be used to obtain $\Re$ for the Cassegrainian telescope, because the aperture shape is similar to that of the Questar. Returning now to Fig. II-9, we used the LE and SENF curves for the long and short exposures, respectively. It is to be noted that the coherence diameter $r_o'$ obtained in the manner described from the 0.63-μm MTF data is a good predictor of the 10.6-μm spot size and spot wander.

A similar correlation, in this case between the 10.6-μm spot wander and the 10.6-μm minimum spot size $\lambda L/r_o$, is shown in Fig. II-11. Here, $r_o$ is obtained through Fried's analysis[6] after computing the 10.6-μm MTF from the long exposure (50-image composite/25 sec) spot distribution. Since the spot wander and coherence diameter are computed from the same data at the same wavelength, the strong correlation is to be expected. However, the relationship between spot wander and the minimum spot size is surprising. Since the spot wander is

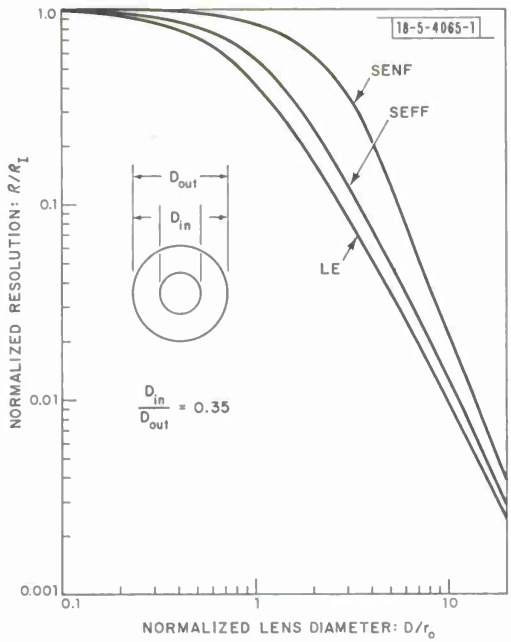


Fig. II-10. Theoretical dependence of atmospherically degraded resolution on coherence diameter.

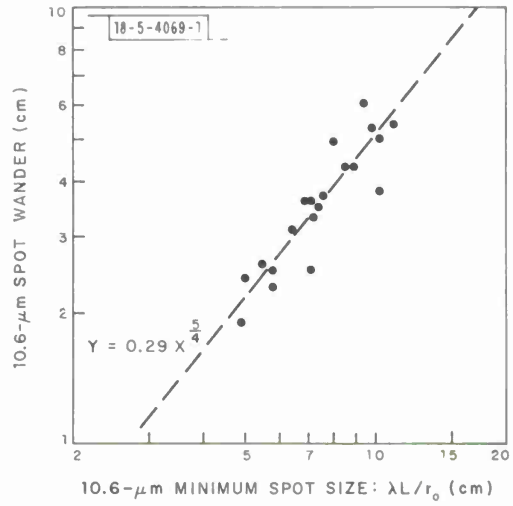


Fig. II-11. Dependence of spot wander on coherence diameter.

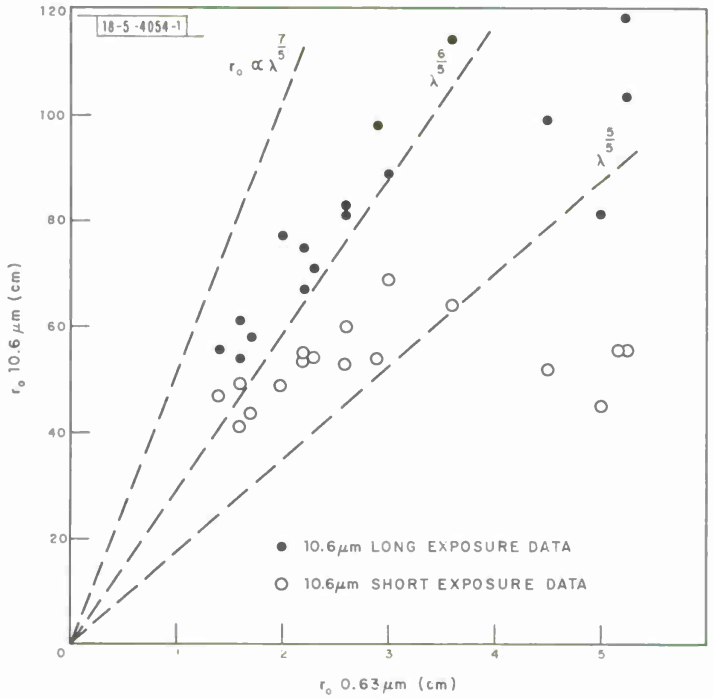


Fig. II-12. Correlation of 10.6- and 0.63-μm coherence diameters.

theoretically proportional to the atmospheric structure constant $C_n$ (Ref. 7) and the minimum spot size is proportional to $C_n^{6/5}$ (Ref. 8), the spot wander should be proportional to the minimum spot size to the 5/6 power. As can be seen in Fig. II-11, the observed dependence is approximately a 5/4 power. This relatively stronger dependence of spot wander than of spot size on $C_n$, which others have also observed,[9] might be explained by variations in the outer scale of turbulence, but simultaneous measurements of spot size, spot wander, $C_n$ and the outer scale have not yet been made to allow verification of this hypothesis.

Perhaps the most significant result of these experiments is the verification of the $\lambda^{6/5}$ dependence of the coherence diameter when the atmosphere is resolution limiting. This is illustrated in Fig. II-12. The $r_o$ (10.6 μm) was computed from the focused spot distribution via the MTF and Fried's analysis as described above for both short and long exposures. The $r_o'$ (0.63 μm) was obtained directly from the short exposure MTF instrument measurements in the same manner. As the seeing deteriorates and $r_o$ becomes smaller, the short- and long-exposure determinations of $r_o$ (10.6 μm) converge. In addition, the ratio of $r_o$ (10.6 μm) to $r_o$ (0.63 μm) converges on $(10.6/0.63)^{6/5} = 30$ in agreement with the predicted wavelength dependence of the coherence diameter.[8] Because the ratio of the wavelengths used is so large, the ratio of the coherence diameters is a very sensitive measure of the wavelength dependence. It is clear from Fig. II-12 that, under conditions of severe atmospheric degradation of resolution, the theoretical dependence is verified. As the seeing improves and $r_o$ increases, the accuracy of the results decreases because the resolution measurement becomes instrument limited and insensitive to $r_o$, as can be seen in Fig. II-10.

4. Summary

This experiment has yielded good measurements of optical coherence at visible and 10.6-μm wavelengths. We have demonstrated the credibility and quantitative usefulness of atmospheric coherence measurements made in the visible (either with the 2-point source apparatus or with the MTF instrument at 0.63 μm) for predicting propagation effects at 10.6 μm. In the process, the diurnal seeing cycle was observed over the Firepond to Groton Firetower test range. Measurements of the focused spot characteristics of a 10.6-μm laser beam were made and a good correlation was obtained between these measurements and coherence measurements made in the visible. The diurnal variation of the 10.6-μm spot size was observed and found to be similar to the seeing cycle in the visible. Several measures of the 10.6-μm spot size were compared. The 10.6-μm spot shape was observed to change from Airy to Gaussian as the seeing deteriorated. The detailed relationship between the 10.6-μm spot size and spot wander was examined and found to deviate significantly from theory, the spot wander being a relatively stronger function of the seeing condition than was the spot size. Finally, the most important outcome of these tests was the verification of the $\lambda^{6/5}$ dependence of the coherence diameter on wavelength.

T. J. Gilmartin
J. Z. Holtz

## REFERENCES


1. Optics Research Reports, Lincoln Laboratory, M. I. T. (1971:2), p. 42, DDC AD-901213-L; (1972:1), pp. 62-68, DDC AD-754939.
2. P. Hariharan and D. Sen, Proc. Phys. Soc. 75, 434 (1960).
3. Optics Research Report, Lincoln Laboratory, M. I. T. (1972:1), pp. 88-89, DDC AD-754939.
4. Ref. 3, pp. 85-86.
5. Optics Research Report, Lincoln Laboratory, M. I. T. (1971:1), pp. 51-56, DDC AD-888823-L.
6. D. L. Fried, J. Opt. Soc. Am. 56, 1372-1379 (1966).
7. R. J. Hull, T. J. Gilmartin and L. C. Marquet, "Laser Beam Wander in Atmospheric Propagation," LTP-7, Lincoln Laboratory, M.I.T. (13 September 1971), p. 10, DDC AD-902040-L.
8. Ref. 6, p. 1372.
9. J. Dowling and P. Livingston, Naval Research Laboratory, Washington, D. C.

## DOCUMENT CONTROL DATA – R&D

*(Security classification of title, body of abstract and indexing annotation must be entered when the overall report is classified)*

| | |
|---|---|
| 1. ORIGINATING ACTIVITY *(Corporate author)*<br>Lincoln Laboratory, M. I. T. | 2a. REPORT SECURITY CLASSIFICATION<br>Unclassified<br>2b. GROUP<br>None |
| 3. REPORT TITLE<br>Optics Research | |
| 4. DESCRIPTIVE NOTES *(Type of report and inclusive dates)*<br>Semiannual Report – 1 July through 31 December 1972 | |
| 5. AUTHOR(S) *(Last name, first name, initial)*<br>Rediker, Robert H. | |
| 6. REPORT DATE<br>31 December 1972 | 7a. TOTAL NO. OF PAGES<br>64<br>7b. NO. OF REFS<br>31 |
| 8a. CONTRACT OR GRANT NO. F19628-73-C-0002<br>b. PROJECT NO. ARPA Order 600<br>c.<br>d. | 9a. ORIGINATOR'S REPORT NUMBER(S)<br>Optics Research (1972:2)<br>9b. OTHER REPORT NO(S) *(Any other numbers that may be assigned this report)*<br>ESD-TR-72-364 |
| 10. AVAILABILITY/LIMITATION NOTICES<br>Approved for public release; distribution unlimited. | |
| 11. SUPPLEMENTARY NOTES<br>None | 12. SPONSORING MILITARY ACTIVITY<br>Advanced Research Projects Agency, Department of Defense<br>Air Force Systems Command, USAF |

13. ABSTRACT

This report covers work of the Optics Division at Lincoln Laboratory for the period 1 July through 31 December 1972. The topics covered are laser technology and propagation, and optical measurements and instrumentation. Additional information on the optics program may be found in the semiannual technical summary reports to the Advanced Research Projects Agency.

14. KEY WORDS

optics
laser technology
thermal blooming
optical devices
optical systems
KC-135
laser radar imaging system